Analysis of the phonon energy transport in the heterostructures of GaInN and GaN

February 2025

Thee Ei Khaing Shwe

Graduate School of Science and Engineering

CHIBA UNIVERSITY

(千葉大学審査学位論文)

Analysis of the phonon energy transport in the heterostructures of GaInN and GaN

February 2025

Thee Ei Khaing Shwe

Graduate School of Science and Engineering

CHIBA UNIVERSITY

Acknowledgments

Research is built on collaborative efforts, much like many other aspects of life. The people who have contributed in various ways, and without their help, support, and guidance, this work would not have been possible. I would like to express my gratitude to everyone who has supported me throughout these years and this journey. First and foremost, I would like to express my deep appreciation to my supervisor, Professor Yoshihiro Ishitani, for providing me with this incredible opportunity, accepting me as his Ph.D student, and for his continuous encouragement and valuable suggestions throughout this journey. I would like to express my sincere gratitude to Professor Kazuhiro Okawa at KAUST University for providing the essential samples for this research. Their support and contribution have been invaluable in advancing this work. I would like to thank Assistant Professor Bei Ma for her invaluable consultation during my research. I would like to extend my heartfelt thanks to Professor Ken Morita, Professor Kenichi Oto, and Associate Professor Masatoshi Sakai for reviewing this thesis.

I would like to thank my seniors and juniors for their support and cooperation in conducting this research. Their assistance and encouragement has been very helpful in this journey. The author would also like to thank Mr. Tatsuya Asaji, a graduate of the master's degree, for his guidance in teaching me how to use the equipment essential for this research. I extend my thanks to Mr. Ryota Kimura, a graduate of the master's degree, and Mr.Yuki Kikuchi, a second-year master's student, for their contributions to our group research and for engaging in valuable discussions that greatly benefited this work. I would also like to thank the doctoral students, second-year master's students, and fourth-year undergraduate students in the same laboratory for their support and collaboration throughout this research. Their contributions and teamwork have been invaluable in achieving the goals of this journey.

Finally, I would like to convey my heartfelt appreciation to my parents and family for their unwavering support in every aspect of my life.

Thee Ei Khaing Shwe

Chiba University, Japan

February 2025

TABLE OF CONTENTS

LIST OF ABBREVIATIONS

LEDs	Light emitting devices
E_2^H mode	E_2(High) mode
A_1^{LO} mode	A_1(LO) mode
A_1^{TO} mode	A_1(TO) mode
E_{E2H}	E_2(High) mode energy
E_{A1LO}	A_1(LO) mode energy
ΔE_{E2H}	The value of total energy shift from difference higher energy to lower energy position of E_2^H mode
ΔE_{A1LO}	The value of total energy shift from difference higher energy to lower energy position of A_1(LO) mode
LOPC	Longitudinal optical phonon plasmon coupling
LO	Longitudinal optical
TO	Transverse optical
GaN	Gallium Nitride
InN	Indium Nitride
GaInN	Gallium Indium Nitride
MOVPE system	Metal organic vapor phase epitaxy system
PL	Photoluminescence
CL	Cathodoluminescence
TRPL	Time-resolved photoluminescence
NR	Non-radiative recombination
x	Mole fraction
3D	Three-dimensional
CW laser	Continuous wave laser
NA	Numerical aperture
CCD camera	Charge-coupled device camera
ND filter	Neutral density filter
Hg lamp	Mercury lamp
DoF	Depth of Field
Si	Silicon
Au	Gold

2D images	Two-dimensional images
α-Al_2O_3	Sapphire
n_e	Electron density
n_e^0	Residual electron density
XRD	X-ray diffraction
AFM	Atomic force microscope
TDs	Threading dislocations
ΔT	Increase in temperature
MBE	Molecular beam epitaxy
E_g	Energy gap
FWHM	Full width at half maximum
IR	Infrared
I_{PL}	PL peak intensity (arb. Unit)
E_{PLP}	PL peak energy (eV)
T	Temperature
ΔT	Change in temperature increase
IR	Infrared

CHAPTER 1

General Introduction

Semiconductors are fundamental components in electronic devices. Without them, the existence of electronic devices would be impossible. In the development of the information technology era in recent years, the heat generated by semiconductor elements has steadily increased yearly. Consequently, a comprehensive understanding of heat energy transport mechanisms in semiconductors has become critical not only for reducing the power consumption of semiconductor elements but also for the enhancement of semiconductor devices.

III-nitride, a semiconductor material, is applied to high-power devices, micro-light-emitting devices (micro-LEDs), and transistors. The device operation characteristics of these devices are degraded by heat energy generation and the increase in temperature [1-3]. Moreover, the heat energy problem is significant in micro-LEDs during operation because of the heat energy generation in a small amount, and thus, higher phonon transport is generally desirable for device efficiency. Consequently, micro-LEDs have several thermal problems because of their size [4], which is described in Figure 1.1. Now, it is widely recognized that heat energy is required to be discussed by means of the quanta of the waves of lattice vibration, that is phonon. It is known that phonons have various interactions with other particle species and physical fields such as radiation. Depending on the size of the sample, diffusive and ballistic phonon transports have been discussed [5,6] as shown in Figure 1.2. The thermal conductivity of gallium nitride (GaN) significantly decreases when its thickness is reduced to 100nm [7]. Analyses of the cumulative thermal conductivity of GaN indicate that 50% of the thermal conductivity is attributed to phonons with mean-free-path values greater than 1μm [8]. As semiconductor devices become increasingly minimized and incorporate multilayer thin film structures, the heat transport properties of these thin films are a crucial part of determining the performance of devices [9]. Therefore, understanding and optimizing these thermal properties is essential for enhancing energy consumption of devices efficiency. In this study, we focus on analyzing the heat transport mechanisms at the active region of device operation, especially in semiconductors, to provide high-efficiency devices through more effective heat dissipation. Figure 1.3 shows the schematic diagram of the longitudinal optical (LO) phonon decomposition process. The LO phonon is the most harmful mode, which is decomposed to the heat energy of acoustic mode, E_2(High) (E_2^H) mode, and transverse optical (TO) modes.

III-nitride semiconductors have a higher interaction of electrons and LO phonons. Figure 1.4 shows the electron-LO phonon interaction strength, which is

defined by a term included in its Hamiltonian E_{LO}. $\left(1/\varepsilon\left(\infty\right)-1/\varepsilon\left(0\right)\right)$. The exclusion of LO phonons from the active regions of devices is considered to have a particularly significant effect on the performance of devices based on III-nitride materials. Here, E_{LO}, $\varepsilon(\infty)$ and $\varepsilon(0)$ represent the LO phonon energy, the relative electric permittivity at the infinite frequency limit, and the static limit, respectively. Additionally, there is a requirement to expel the acoustic phonons generated by the decomposition of LO-phonons to reduce the regeneration of LO phonon from the other mode phonons. Therefore, the analysis of the generation and decomposition of LO phonons inducing acoustic phonon generation is a crucial issue for the further control of electron-LO phonon interactions.

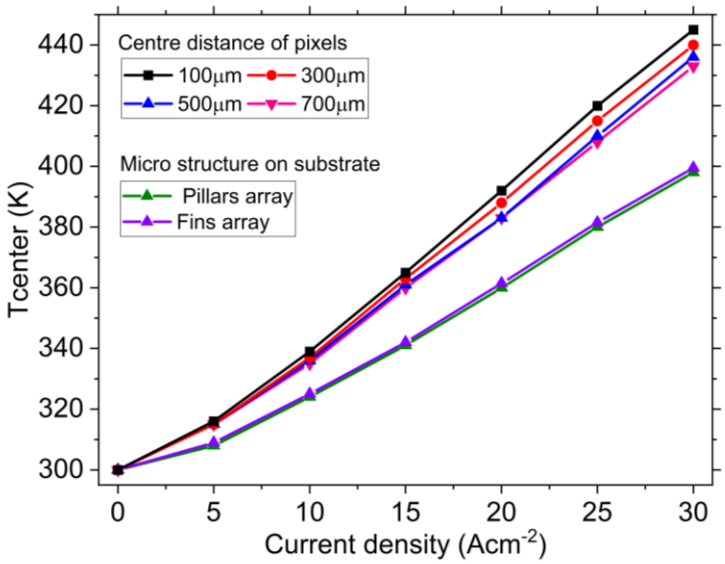

Figure 1.1. Surface temperature of the center LED vs the current density, for center distances of 100 μm, 300 μm, 500 μm, 700 μm and flat substrate, compared with the results obtained for substrates with arrays of pillars and fins, for the center distance of 500 μm [4].

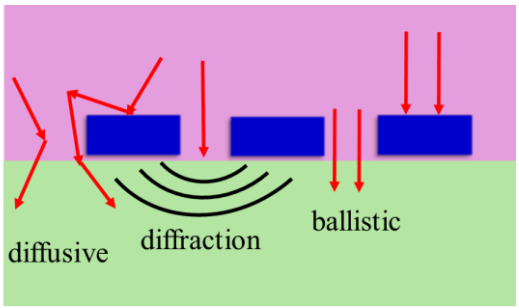

Figure 1.2. Various processes of phonon transport types: ballistic and diffusive transport and diffraction.

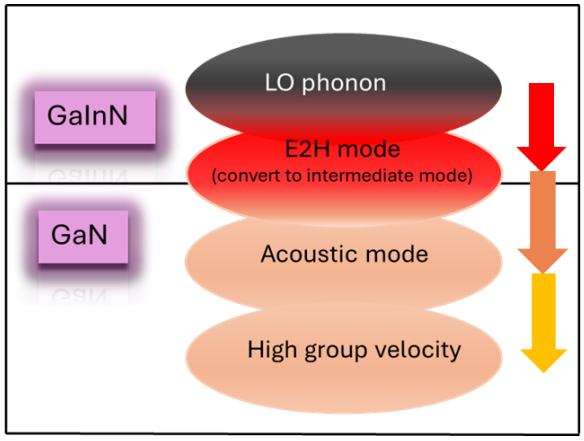

Figure 1.3. A Schematic diagram of LO phonon decomposition process.

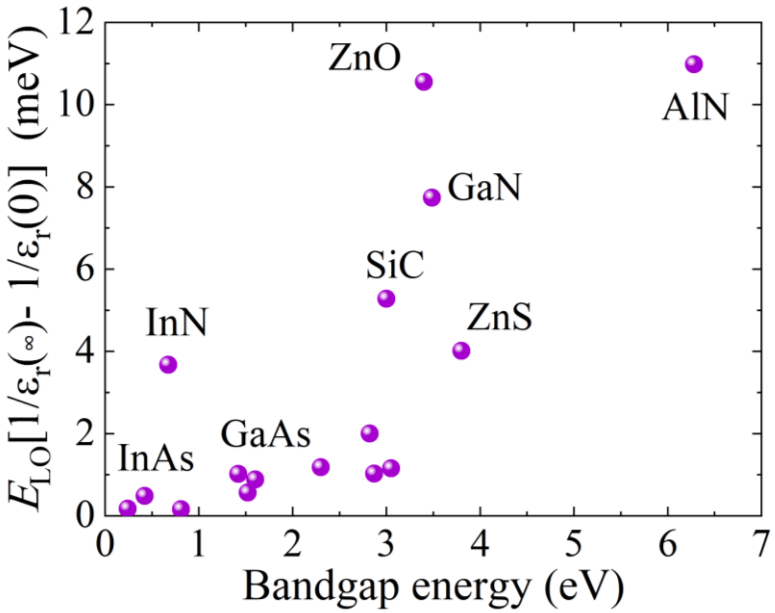

Figure 1.4. Interaction between LO phonon and the electric field in semiconductors [37].

III-nitride semiconductors are mostly grown on heterogeneous substrates such as sapphire and silicon. That induces misfit dislocations, threading dislocations, and complex defects [11-12]. In this study, GaN and indium nitride (InN), are mainly focused. The band gaps are 3.4 eV and 0.63 eV, respectively, at room temperature [13]. On the other hand, the $Ga_{1-x}In_xN$ alloy exhibits a wide lattice parameter range based on the lattice mismatch of 11% between InN and GaN [13-15]. The varying crystal growth temperatures lead to localized compositional fluctuations. These fluctuations can lead to distortion and lattice defects. Some of the lattice defects induce radiative

recombination of carriers, which yields heat energy or phonons. The increased density of phonons and an increase in the occupancy of phonon states cause further non-radiative recombination (NR), resulting in additional heat generation. However, studies on the phonon transport properties at heterointerfaces have remained limited [16]. In addition, the LO phonons have a significant impact on device characteristic degradation due to temperature increases in nitride semiconductors [17]. Therefore, observing and analyzing of each vibration mode is crucial for understanding and controlling these effects.

The observation of the nonradiative recombination centers can be investigated by using electron-induced luminescence (cathodoluminescence (CL)) images, which result in a dark spots region in CL. However, direct imaging of carrier density has not been achieved despite the impact on the luminescence intensity. It can be clearly shown in Figure 1.5 (c), which is CL imaging of the GaInN layer. Figure 1.5 (a) (b) was PL mapping imaging of the GaInN layer; the dashed lines in these figures indicated the common observation area of the CL and PL mapping images. The CL image exhibits high intensity at the white circle, which agrees with the PL image. At the left-hand side dark-blue circle, the intensity takes a local maximum though the PL intensity takes a local minimum. In this region, generated carriers are estimated to be transported outside the observation region. At the right-hand-side dark-blue circle, a weak CL spot is observed, where the PL peak energy of the GaInN layer takes a local minimum, whereas that of the GaN layer takes a local maximum. Strain relaxation or In segregation [36] is estimated to take in this region. In regions marked by light-blue circles, NRs are thought to dominate the PL and CL intensities. At some CL dark spots, the PL intensity does not take a local minimum. To interpret this phenomenon, it is required to analyze the carrier transport, radiative and nonradiative recombination processes [29].

As, thermal energy and carrier transport processes have a significant impact on carrier recombination processes, simultaneous imaging analysis of luminescence, temperature, and carrier density are essential features for a comprehensive understanding of PL and Raman imaging. The PL emission efficiency, which is defined as the luminescence intensity per electron, is especially important in crystal fields with nonuniformity in alloy composition and defect density. The local carrier density was determined through the analysis of longitudinal optical (LO) phonon-plasmon coupling (LOPC) modes using microscopic Raman scattering measurements [31, 34-35]. As it is known that electron density is high in regions of local minima of potential energy, the

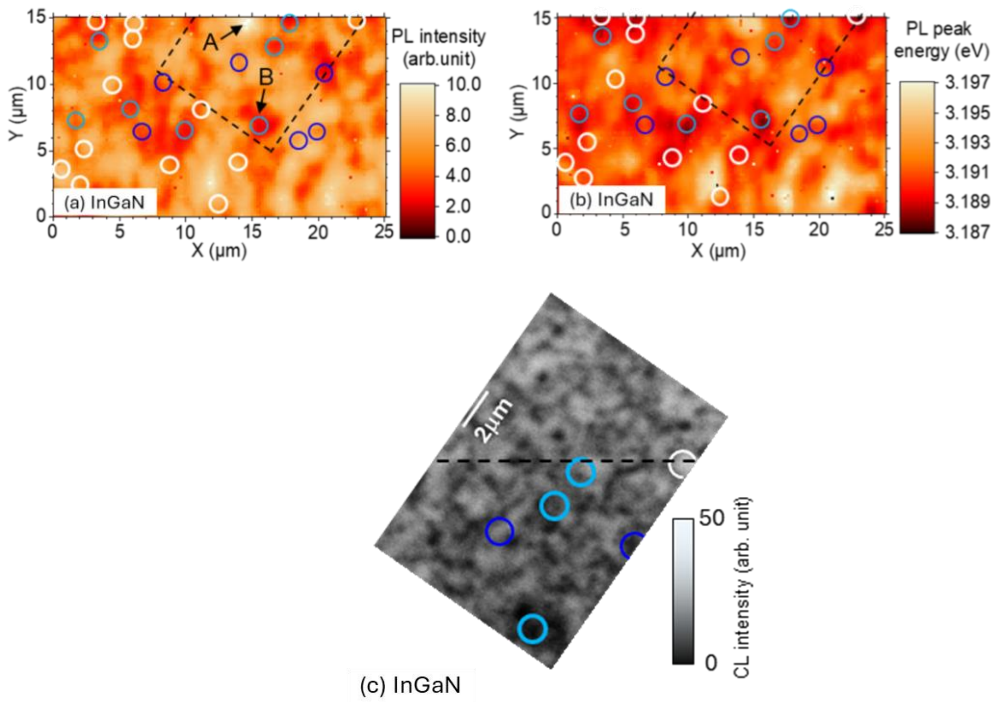

Figure 1.5. The $Ga_{0.95}In_{0.05}N$ layer of (a) PL intensity, (b) PL peak energy, and CL intensity. Note that the region below the dashed line is observed in PL imaging. The six circles in CL imaging represent the respective same region in PL imaging [29].

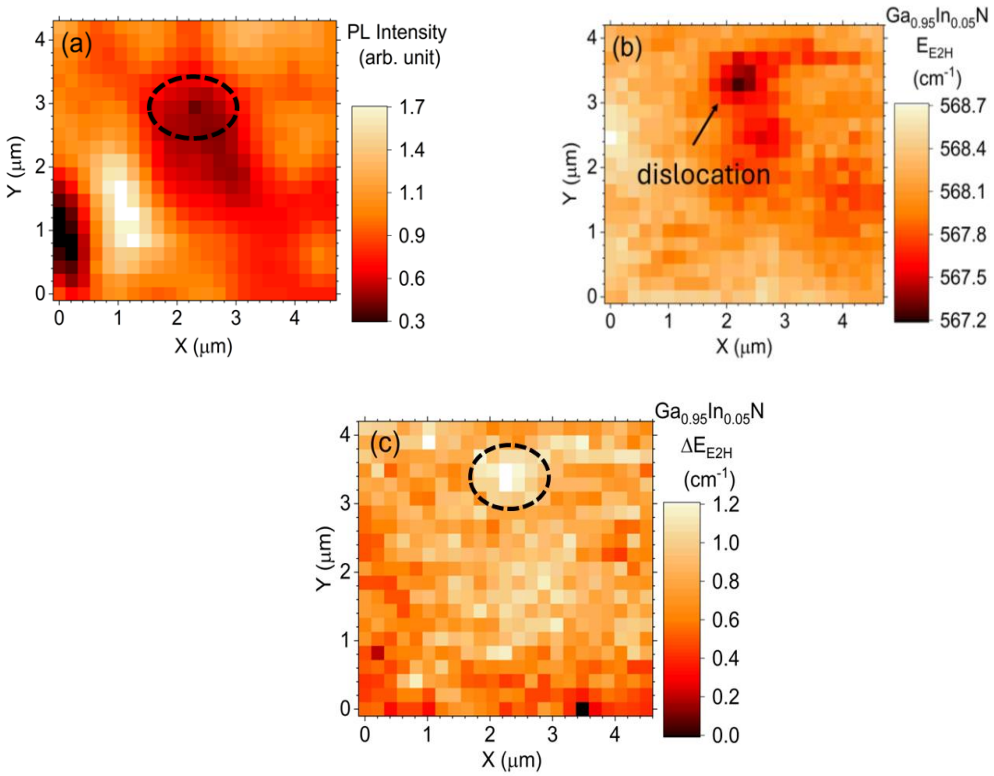

Figure 1.6. (a) Imaging of PL intensity of $Ga_{0.95}In_{0.05}N$ (b) Imaging of E_2^H modes energy using the 325 nm laser with power 14 mW (c) decrease ΔE_{E2H} energy mode with increasing incident laser power (7 mW – 14mW).

electron density is thought to be fluctuated by local fluctuation of alloy composition, stress, temperature, and so on. Local fluctuation of temperature is considered to induce local strain, potential minima, and fluctuation of the kinetic energy of carriers. In addition, local analysis of the correlation of the images of the temperature obtained from the Raman spectroscopy and photoluminescence has a small mismatch from the reported [20] as shown in Figure 1.6. The local analysis of the correlation among temperature, electron density, and photo-emission efficiency was investigated in this study. Selective heating and simultaneous observation of phononic and photonic properties are studied to contribute to the analysis of carrier dynamics in inhomogeneous crystals.

In this research, the combination analysis of the two-dimensional images of phonon mode energies, as well as PL peak energies and intensities, localized temperature increases are observed in the vicinity of crystal defects. When the carriers are photoexcited to a high energy level above the band edge, the carriers generate phonons through the carrier energy relaxation inside the bands. Therefore, the local temperature increases in this process. The increase in temperature can be detected by Raman scattering measurements [16, 20, 29, 30]. Raman imaging was performed by controlling the generated heat energy, the heating position, and the measurement position through the simultaneous irradiation of two lasers (pump and probe techniques). The investigation of thermal energy transport imaging within thin films and across interfaces was conducted using a microscopic Raman measurement system with a double laser system [16, 30]. The transport of thermal energy across interfaces is a key factor in determining the accumulation of heat energy in the active regions of electronic and photonic devices.

There are five chapters in this thesis. Chapter two introduces the measurement system and experimental method. Chapter three demonstrates the PL emission efficiency analysis by integrating analysis of Raman imaging of E_2^H mode and A_1^{LO} mode in a heterostructure of $Ga_{0.95}In_{0.05}N$ and GaN. Chapter four shows the details of analysis of phonon transport at $Ga_{1-x}In_xN$ and GaN heterointerface. Chapter five describes the mechanism of the ratio of energy decrease of ΔE_{A1LO} by ΔE_{E2H} mode of Fe-doped GaN and bulk GaN. Chapter six expresses the conclusions of the present research.

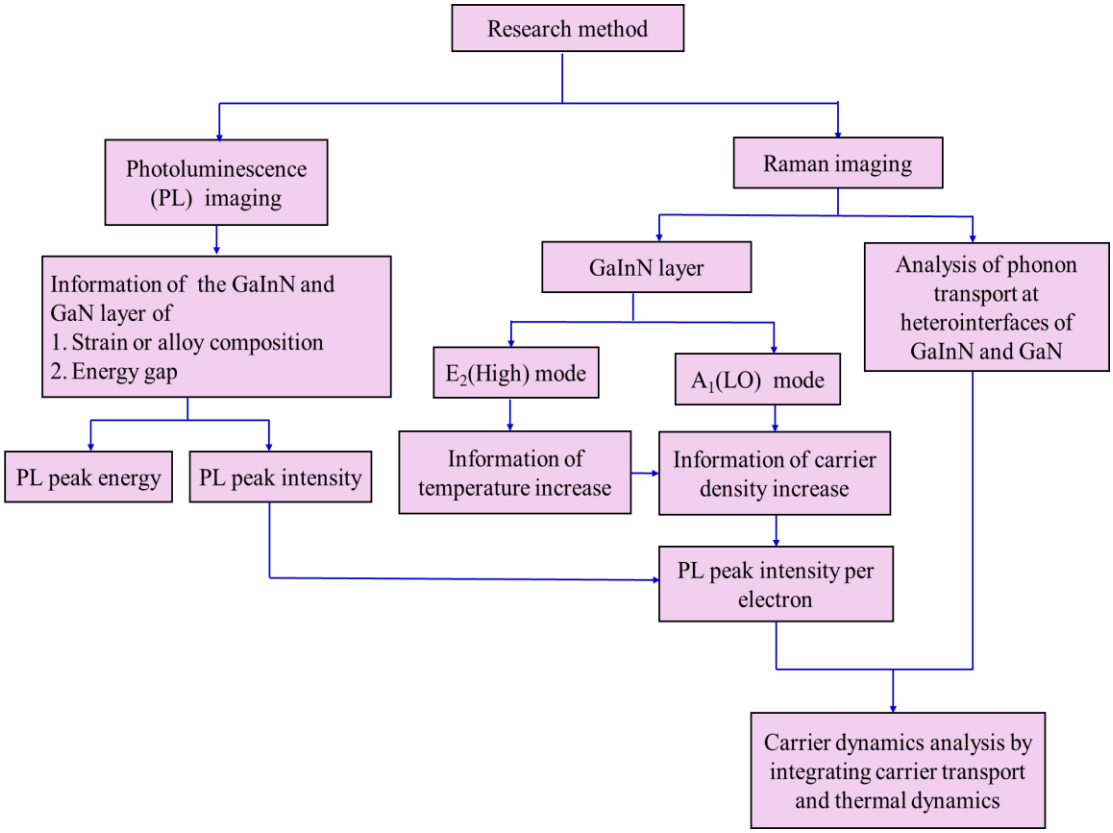

Figure1.7. Research method.

References

[1] M. Baira Jabbari, H. Maaref, R. Mghaieth, Physica E 104, 216–222, (2018).

[2] C. Gaqui` ere, H. Maaref, Hole trap, J. Phys. Chem. Solid. 132, 157–161, (2019).

[3] M.S. Ferdous, X. Wang, M.N. Fairchild, S.D. Hersee, Appl. Phys. Lett. 91, 231107, (2007).

[4] S. Fang, W. Wang, J. Liang, Z. Liang, Y. Qin, J. Lv, AIP Advances 7, 015209 (2017).

[5] T.. E. Beechem, A. E. McDonald, Elliot J. Fuller, A. Alec Talin, C. M. Rost, J. P. Maria. J. T. Gaskins, P. E. Hopkins, A. A. Allerman, Appl. Phys. 120, 095104, (2016).

[6] K. Oki, B. Ma, Y. Ishitani Phys. Rev. B 96, 205204, (2017).

[7] B. A. Danilchenko, T. Paszkiewicz, S. Wolski, A. J. zowski, T. Plackowski, Appl. Phys. Lett. 89, 061901, (2006).

[8] T. E. Beechem, A. E. McDonald, E. J. Fuller, A. A. Talin, C. M. Rost, J. P. Maria, J. T. Gaskins, P. E. Hopkins, A. A. Allerman, J. Appl. Phys. 120, 095104, (2016).

[9] M. Zhanghu, B. R. Hyun, F. Jiang, and Z. Liu, AIP Advances, Vol. 30, Issue 6, pp. 10119, 10125 (2022).

[10] Y. M. Chang, C. T. Chuang, J. App. Phys. 102, 083540 (2007).

[11] M. Iwaya, T. Yamamoto, D. Iida, Y. Kondo, M. Sowa, H. Matsubara, K. Ishihara, T. Takeuchi, S. Kamiyama, I. Akasaki. J. Appl. Phys. 54, 115501, (2015).

[12] T. Sugiyama, Y. Kuwahara, Y. Isobe, T. Fujii, K. Nonaka, M. Iwaya, T. Takeuchi, S. Kamiyama, I. Akasaki, H. Amano, APEX 4, 015701, (2011).

[13] J. Wu, W. Walukiewicz, K. M. Yu, J. W. Ager III, S. X. Li, E. E. Haller, H. Lu, and W. J. Schaff: Sol. Stat. Commun. 127, 411, (2003).

[14] Y. Ishitani, M. Fujiwara, T. Shinada, X. Wang, S.-B. Che, A. Yoshikawa, Phys. Sat. Sol. C 4, 2428, (2007).

[15] Y. Zhao, H. Wanga, X. Gong, Q. Li, G. Wu, W. Li, X. Li, G. Du, J. Lumin. 186, 243246, (2017).

[16] S. Okamoto, N. Saito, K. Ito, B. Ma, K. Morita, D. Iida, K. Ohkawa, Y. Ishitani Appl. Phys. Lett. 116, 142107, (2020).

[17] Y. Kawakami, K. Omae, A. Kaneta, K. Okawmoto, T. Izumi, S. Saijoou, K. Inoue, Y. Narukawa, T. Mukai, S. Duita, Phys. Status Solidi A, 183, 41, (2001).

[18] Y. Kawakami, K. Omae, A. Kaneta, K. Okawmoto, T. Izumi, S. Saijou, K. Inoue, Y. Narukawa, T. Mukai, Fujita Sg, Phys. Status Solidi A , 183, 41, (2001).

[19] K. Katayama, K. Sugai, Y. Inagaki, T. Sawada, J. Appl. Phys., 91, 1074, (2002).

[20] M. BouSanayeh, P. Brick, W. Schmid, B. Mayer, M. Müller, M. Reufer, K. Streubel, J. W. Tomm, G. Bacher, Appl. Phys. Lett., 91, 041115, (2007).

[21] H. Murotani, K. Shibuya, A. Yoneda, Y. Hashiguchi, H. Miyoshi, S. Kurai, N. Okada, K. Tadatomo, Y. Yano, T. Tabuchi, K. Matsumoto, Y. Yamada, Jpn. J. Appl. Phys., 58, SCCB02, (2019).

[22] L. Marona, D. Schiavon, M. Baranowski, R. Kudrawiec, I. Gorczyca, A. Kafar, P. Perlin, Sci. Rep., 10, 1235, (2020).

[23] S. J. Henley, D. Cherns, J. Appl. Phys., 93, 3934, (2003).

[24] J. Lähnemann, V. M. Kaganer, K. K. Sabelfeld, A. E. Kireeva, U. Jahn, C. Chèze, R. Calarco, O. Brandt, Phys. Rev. Appl., 17, 024019, (2022).

[25] S. Kurai, A. Wakamatsu, Y. Yamada, Jpn. J. Appl. Phys., 58, SCCB13, (2019).

[26] P. A. Crowell, D. K. Young, S. Keller, E. L. Hu, D. D. Awschalom, Appl. Phys. Lett., 72, 927, (1998).

[27] A. Kaneta, K. Okamoto, Y. Kawakami, S. G. Fujita, G. Marutsuki, Y. Narukawa, T. Mukai, Appl. Phys. Lett., 81, 4353, (2002).

[28] A. Kaneta, M. Funato, Y. Kawakami, Phys. Rev. B, 78, 125317, (2008).

[29] T. Nakayama, K. Ito, B. Ma, D. Iida, M. A. Najmi, K. Ohkawa, Y. Ishitani, Mater. Sci. Semicond. Process., 150, 106905, (2022).

[30] M.Kuball, S. Rajasingam, A. Sarua, M. J. Uren, T. Martin, B.T. Hughes, K. P. Hilton, R. S. Balmer, Appl. Phys. Lett., 82,124, (2003).

[31] M. Kuball, IEEE Trans. Device Mater. Reliab. 16, 667–684, (2016).

[32] R.J. Simms, J.W. Pomery, M.J. Uren, T. Martin, M. Kuball, Appl. Phys. Lett. 93, 203510, (2008).

[33] C. Hodges, J. Pomeroy, M. Kuball, J. Appl. Phys. 115, 064504, (2014).

[34] M. Kawase, J. Suda, Vib. Spectrosc., 118, 103331, (2022).

[35] G. Matínez-Criado, A. Cros, A. Cantarero, P. Ambacher, C. R. Miskys, R. Dimitrov, M. Stutsmann, J. Smart, J. R. Shealy, J. Appl. Phys.,90, 4735, (2001).

[36] F.A. Ponce, S. Srinivasan, A. Bell, L. Geng, R. Liu, M. Stevens, J. Cai, H. Omiya, H. Marui, S. Tanaka, Phys. Status Solidi B, 40, 10.1002, 273 (2003).

[37] Y. Ishitani, K. Oki, H. Miyake, J.J. Appl.Phys. 58, SCCB34, (2019).

CHAPTER 2
Measurement System and Experimental Method

Abstract

The basic experimental setup of the present Raman and PL spectroscopy, as well as the measurement systems and the measurement methods, are expressed. Especially the present techniques are designed to capture lateral and cross-interface phonon transport, which is essential for understanding phonon dynamics in the material. The key experimental factors, such as resolution constraints, data accuracy, and sources of measurement uncertainty are expressed.

2.1. Measurement System of Raman Spectroscopy

Raman spectroscopy is known as a method to analyze the crystal structure, alloy composition, and strain by means of vibrational lattice frequency. In this study, a confocal Raman microscopic instrument using a double laser system was used. This study utilized the three-dimensional (3D) laser Raman spectroscopy system (Nanofinder30, Tokyo instruments). The measurement system of the Raman spectroscopy is shown in Figure 2.1. In this study, two types of continuous wave (CW) lasers were utilized, which are 532 nm second harmonic radiation of a Nd: YAG laser (Showa Optonix) and a 325 nm He-Cd laser (Kimmon Kohwa). The 325 nm He-Cd laser was utilized as the excitation light source in PL measurements and the heating on probing light in Raman scattering analysis. The objective lens of numerical aperture (NA) is 0.47, 40x (Thorlabs, LMU-40x-NUV) was used. The laser spot diameter was approximately 0.69 μm for the 532 nm laser and 0.42 μm for the 325 nm laser. In the simultaneous irradiation of the two cases, the respective spot diameters were 0.69 μm for the 532 nm light, while the 325 nm light was diffused to a diameter of approximately 7 μm. The focal length of the monochromator was 81.6 cm, and a diffraction grating in the spectrometer was selected from three types of groove counts: 600 G/mm, 2400 G/mm, and 3600 G/mm. In the measurement system, the wavelength range and resolution were varied according to the groove count of the diffraction grating. The 600 G/mm of groove count was used for low resolution and wide spectral range. The 2400 G/mm grating offered better resolution than 600 G/mm and provided a moderate level of wavelength separation. The groove count of 3600 G/mm was utilized for the high spectral resolution and narrow spectral range. In this study, the grating of 600 G/mm was used for PL measurements by using the 325 nm laser and, the 3600 G/mm grating was used for Raman spectroscopy for 325 nm laser, and the 2400 G/mm was used for Raman spectroscopy using the 532 nm laser. The optical signals were captured from a charge-coupled device (CCD) camera (ANDOR). For the simultaneous irradiation measurements by using two lasers (532 nm for the Raman signal probe laser and 325-nm for the heating laser), where a harmonic reflector was utilized to reflect the 325 nm laser light and to pass through the 532 nm laser light before the entrance of these lasers into the objective lens. The light path for the basic Raman measurement setup is shown in Figure 2.1. The laser light emitted from the laser source passes through an interference mirror and enters the Nanofinder30 system. The laser light passes through

the neutral density (ND) filter and beam expander, which was expanded by the beam expander. After that, the light passed through a mirror and an objective lens and was focused onto the sample. The scattered light from the sample was dispersed by the spectrometer after reducing the Rayleigh scattering light by an edge filter. The light then passed through the diffraction grating and was detected by the CCD camera, where photons are captured and converted into electrical signals. This process reads out and produces the detected spectral information as an output.

2.2. Sample Stage and Mapping

An XYZ-axis piezo stage (LJ014M01, Nano control) was installed on the stage for positioning the microscope sample, with fine adjustments made using a controller (NCM6301C, Nano control). The sample stage was composed of a coarse adjustment stage, a piezoelectric stage, a rotation stage, and a goniometer stage from the bottom. The coarse stage enables manual adjustment on the XYZ axis, and the XY axis, in particular, is equipped with a micrometer. The piezoelectric stage can be controlled from the software in an area of 100 μm square with a resolution of a few tens of nanometers on the XYZ axis. The rotation stage can be manually adjusted to the direction of the sample, and the goniometer stage enables manual adjustment of the sample's inclination. Additionally, the mapping measurement was controlled automatically by the software using the piezo stage. Therefore, the measurement of the mapping area was specified by the measurement size and step size resolution. The piezoelectric stage was automatically moved to perform measurements. During mapping measurements, the microscopy system was covered with an acrylic plate which is thermoplastic material to prevent changes in the surrounding temperature. The temperature in the sample chamber was controlled by following an air, the temperature of which was controlled 23℃ (± 0.1℃). The surrounding temperature of the whole system was controlled at 22 ~ 23℃.

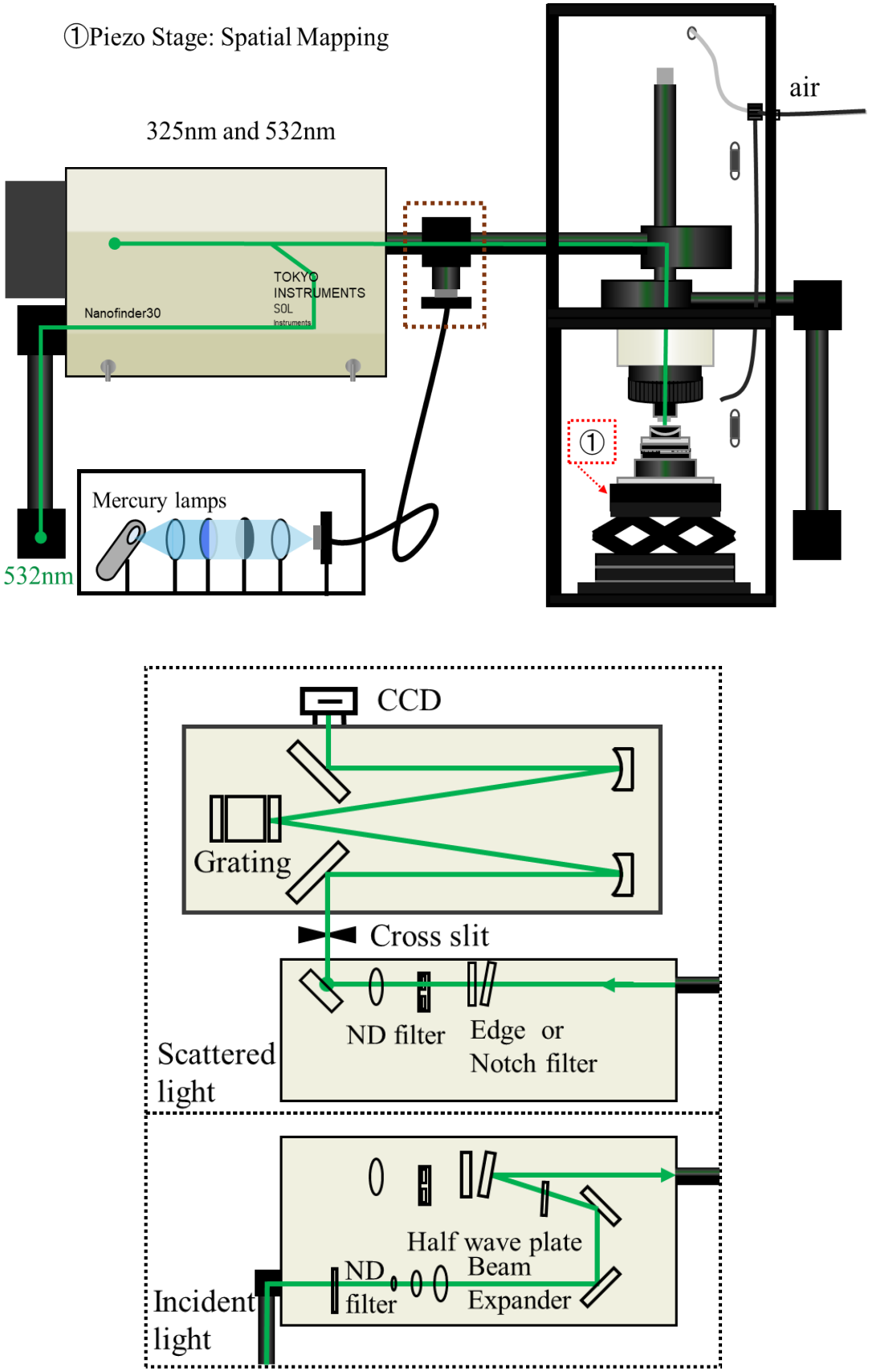

Figure 2.1. Measurement system of Raman Spectroscopy.

2.3. Spatial Resolution

The confocal Raman spectroscopy has the ability to spatially resolve the same diameter at the laser spot on the sample when the observation wavelength is the same as that of the laser, enabling analysis of the sub-micrometer size structure of the sample. It is important to take into account spatial averaging when analyzing temperatures measured by confocal Raman spectroscopy which is determined by the optical resolution of the measurement system. In this system, the monochromator had a cross-slit, which worked as the confocal slit. The diameter of the slit was controlled in a range of 50 μm ~ 150 μm. There are two types of spatial resolution, which are lateral (XY) resolution and depth (Z) resolution. The schematic diagram of spatial resolution is shown in Figure 2.2. The lateral (XY) resolution determined by the specification of the objective lens is expressed with Equation 2.1 [1].

$$\gamma_{\text{lateral}} = \frac{0.61\lambda}{NA} \tag{2.1}$$

where λ is the wavelength of the laser light used, and γ_{lateral} is the lateral resolution of the XY plane in nanometers.

The diameter and focal length of the achromatic lens in front of this slit was 25-mm and 150 mm, respectively. When we use the objective lenses with NA values of 0.95 and 0.47 with 532 nm laser wavelength, the diameter of the image of the object spot is estimated to be 0.34 μm and 0.69 μm, respectively. As for the focal length of the lens in front of the split is 150 mm, the diameter of the image on the entrance slit are 9.6 μm and 19 μm for the respective objective lens according to Equation 2.1. The 50 μm is approximately 2.5 times the 19 μm. Therefore, the spatial resolution is determined by the NA value of the objective lens when the cross diameter is less than 50 μm. The axial resolution in the z-direction of the spatial resolution, which is related to the depth of field (DoF), is expressed by Equation 2.2 [1].

$$\gamma_{\text{axial}} = \frac{0.61\lambda}{NA} * \sqrt{1 + \left(\frac{\lambda}{\pi * \left(\frac{0.61\lambda}{NA}\right)^2}\right)^2} \tag{2.2}$$

where λ is the wavelength of the laser light used, and γ_{axial} is the axial resolution (or depth resolution) in the z-direction.

In confocal Raman spectroscopy measurement, the axial spatial resolution is primarily determined by the absorption depth of incoming and scattering light rather than the DoF when the laser wavelength is used in the above bandgap.

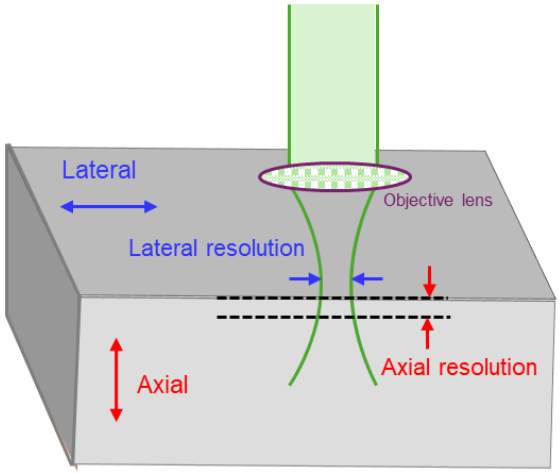

Figure 2.2. Schematic diagram of spatial resolution.

2.4. Wavenumber Calibration

In the Raman scattering measurement system, wavenumber calibration is essential to ensure the precision and accuracy of the spectral data obtained. The primary purpose of this calibration is to correct any discrepancies between the detected and the actual wavenumbers from the molecular vibrations. The energy shift of the scatter light from the irradiated laser (Rayleigh light) is observed in Raman spectroscopy. When the Raman shift is high, it is impossible to obtain both the signals of the Raman scattering and Rayleigh scattering on the CCD sensor array without scanning the monochromator grating. In addition, wavelength accuracy cannot be guaranteed due to changes in the surrounding environment, such as room temperature, which are caused by long-term measurements. Therefore, the specification of the lamp neon or mercury lamps, suitable for a measurement depends on the objective phonon mode energy. Figure 2.3 (a) shows the fluctuation of the 7^3S_i-6^3P_2 (5460.7 °*A*) lines of the mercury lamp and the difference in the value of fluctuation of the wavelength expressed in Figure 2.3 (c). Figure 2.3 (b) shows the resolution of the peak energy is high enough. The fluctuation of the

wavelength of the mercury lamp line is attributed to the fluctuations in the measurement environments.

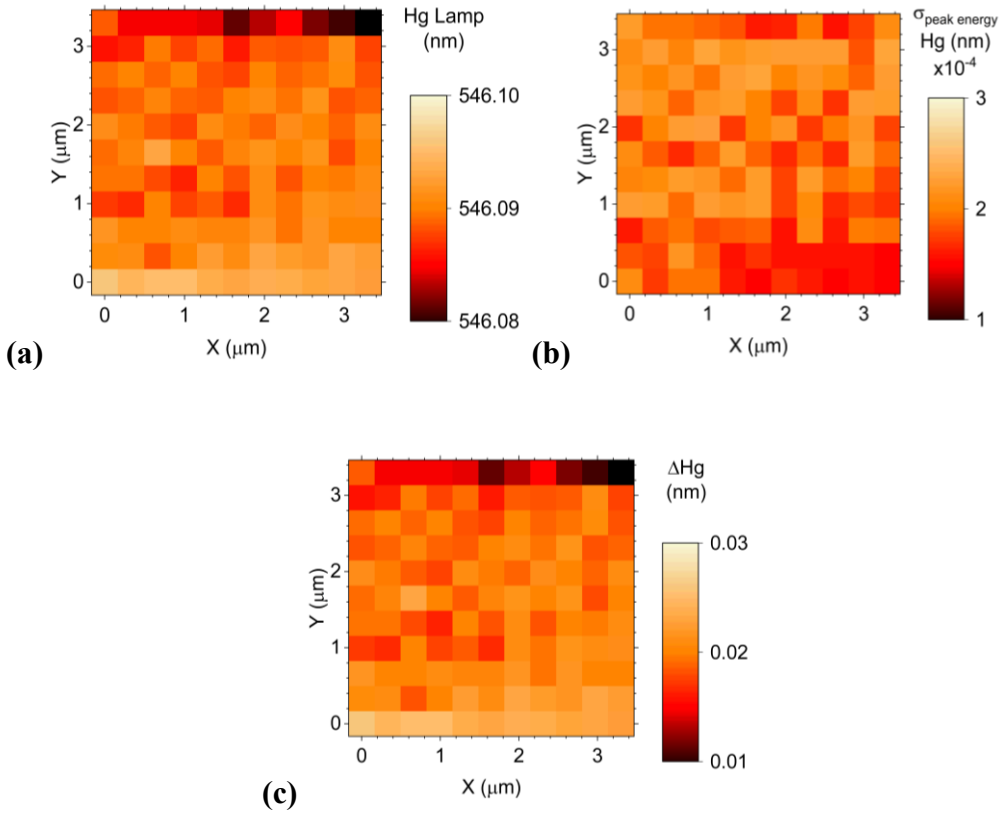

Figure 2.3. Mapping image of a mercury lamp of (a) peak energy, (b) standard deviation of the peak energy, and (c) the value of the calibration of wavelength at the GaN layer with 532 nm laser excitation.

2.5. Wavenumber Resolution

The wavenumber resolution depends on the slit width of the spectrometer and the distance between the CCD devices, the pixel size of the CCD camera, the grooving period of the grating of the monochromator, and the focal length of the monochromator. The wavenumber resolution $d\lambda$ is expressed by

$$d\lambda = dx\left(\frac{d}{f}\right)\cos[\tan^{-1}\frac{\frac{\lambda}{d}}{\sqrt{(1+cos\alpha)^2+\sin^2\alpha-\left(\frac{\lambda}{d}\right)^2}}-\varphi] \quad (2.4)$$

where d is the ruling period, dx is the slit width and α is the angle of the incident and outflow light directions.

2.6. Sensitivity Calibration

The light scattered by the sample is detected using mirrors, filters, a grating, and a CCD camera. Sensitivity calibration is required to ensure the accurate signal intensity for each wavelength. A halogen lamp (Philips, FCR A1/215) was used to calibrate the sensitivity of the measurement system equipped with an objective lens and a diffraction grating. This lamp has a color temperature of 3300 K. The theoretical formula for a halogen lamp was assumed to subject to Planck's blackbody radiation formula$I_{bbr}(E)$ as shown in Equation 2.5.

$$I_{bbr}(E) = \frac{2\hbar v^3}{c^2} * \frac{1}{e^{\frac{\hbar v}{kT}} - 1} \tag{2.5}$$

where, $I_{bbr}(E)$ is the spectral radiance of the blackbody radiation, $\hbar$is the Plank's constant, v is the frequency of the radiation, c is the speed of light in a vacuum, k is the Boltzmann's constant, and T is the color temperature of 3300 K of the halogen lamp.

The spectrum observed for the lamp is I_{Hal}, and the light intensity as a function of photon energy is set to be

$$I_{Hal} = I_{bbr}(E)dE * \eta(\mathrm{E}) \tag{2.6 a}$$

$$I_{Hal} = I_{bbr}(E) * (\frac{hc}{\lambda^2}) \left[dx * \frac{d}{f} * \cos\left\{ \tan^{-1}\left(\frac{\frac{\lambda}{\mathrm{d}}}{\sqrt{(1+cos\alpha)^2 + sin^2\alpha - (\frac{\lambda}{\mathrm{d}})^2}} \right) - \emptyset \right\} \right] \eta(\mathrm{E}) \tag{2.6 b}$$

where, dx is the slit width, *d* is the ruling period of the diffraction grating, *f* is the focal length of the spectrometer, $\eta(E)$ is denoted as the sensitivity and α is the angle of the optical path of the diffraction grating.

The spectral sensitivity $\eta(E)$ calibration can be calculated by using equation (2.7). When the equation is rearranged using the halogen lamp measurement data, I_{Hal}, the sensitivity data $I_0(E)$ is expressed by Equation 2.7.

$$\eta(\mathrm{E}) = I_{Hal}/I_{bbr}(E)dE \tag{2.7 a}$$

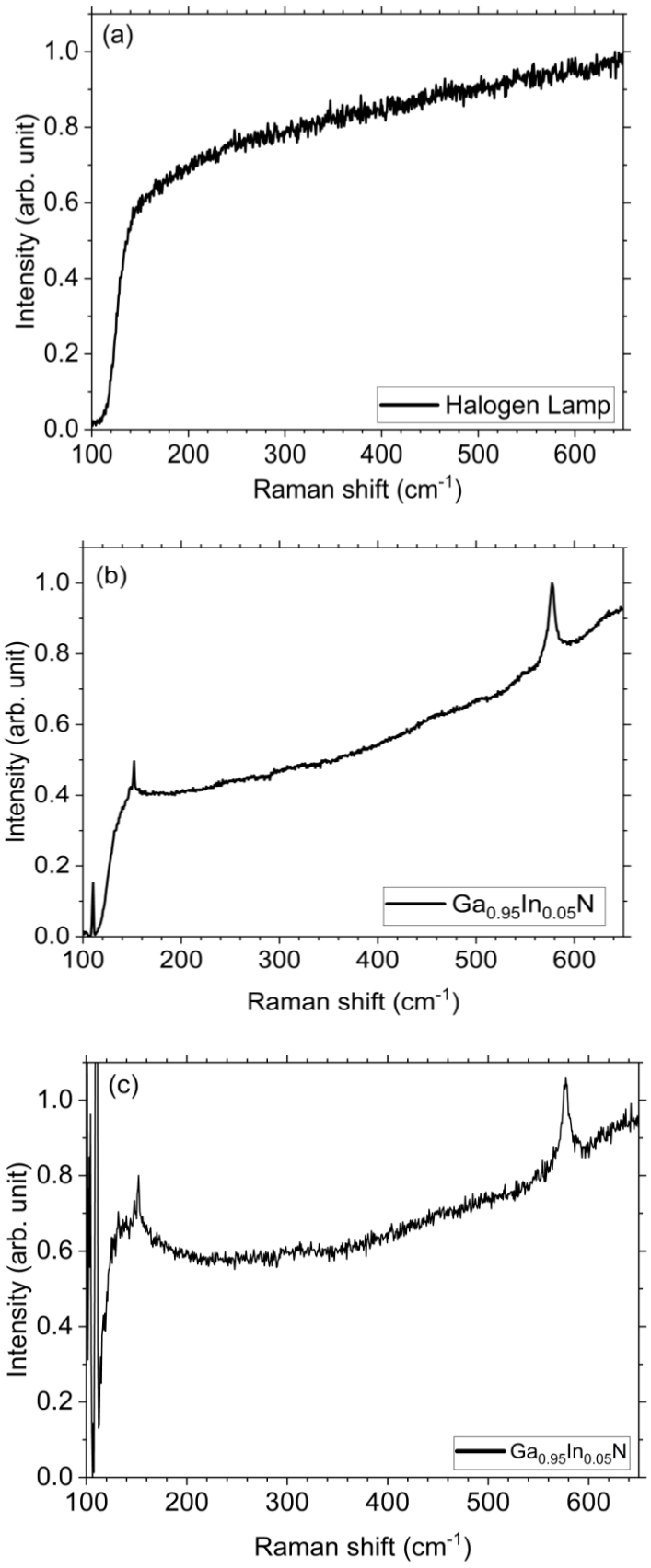

Figure 2.4. The emission spectrum of the (a) halogen lamp, (b) before, and (c) after sensitivity calibration of a Raman scattering spectrum.

$$\eta(\mathrm{E}) = \frac{I_{Hal}\left(\frac{\lambda^2}{hc}\right)}{I_{bbr}(E) * \left[\frac{d}{f} * \cos\left\{\tan^{-1}\left(\frac{\frac{\lambda}{\mathrm{d}}}{\sqrt{(1+cos\alpha)^2 + sin^2\alpha - (\frac{\lambda}{\mathrm{d}})^2}}\right) - \emptyset\right\} dx\right]} \quad (2.7\ \mathrm{b})$$

This is the $In_{0.05}Ga_{0.095}N$ of the Raman spectrum before and after sensitivity calibration, shown in Figure 2.4. The measurement conditions, that is, spectrometer entrance slit (pinhole), CCD center, track height, and wavenumber range, are all the same calibrations.

2.7. CCD Camera

In this study, Raman scattering light was observed using a CCD camera (ANDOR, DU420A-B). The CCD has a structure is 1024 horizontal and 256 vertical light-receiving elements, with a pixel size of 26 μm. Therefore, 1024 data points are obtained during measurement. To reduce the noise, only some rows of vertical pixels were used. In measurements, the center of the CCD was set up to 130 ~145 and the track height was set up to 10. The sensitivity of the CCD was determined by the system readout rate and preamplifier setting, and the signal intensity is the value converted from the number of photoelectrons. The noise of the CCD camera is determined as the base label, and when the system readout rate was 0.03 MHz, and the preamplifier gain

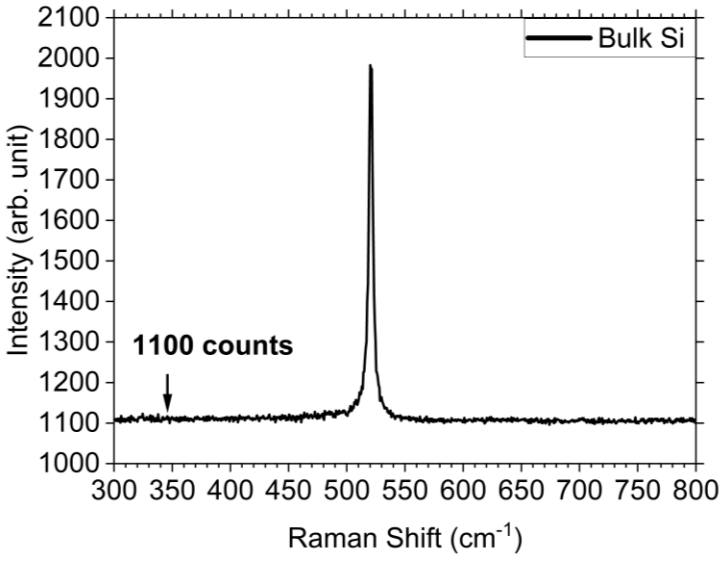

Figure 2.5. Bulk Si with Raman spectroscopy with 325 nm laser excitation.

setting was 1x, the noise of the CCD camera was approximately 1100 counts. Figure-2.5 expresses the noise level of the CCD camera starting from the 1100 counts, measured using bulk silicon with a laser power of 5 mW and 5 seconds exposure time with a one-time accumulation under the 325 nm laser excitation in Raman spectroscopy.

2.8. Patterning on the Sample Surface

A gold sputtering mask was deposited onto the sample to obtain a precise position for phonon transport measurement. The (Mikasa, MA-20) was utilized for exposure, and the magnetron sputtering (Labotec, LA-S2020) system was used for sputtering. The entire mask was 10 mm square, and the small pattern was 20 μm square. Figure 2.6 shows an example image of the patterned sample. The patterned structure of the sample enabled precise determination of the measurement locations and repeating measurements at the same point. Moreover, the thickness of the deposited metal was approximately 20 nm, and the PL peak intensity (I_{PL}) at that location shows a reduced intensity as shown in Figure 2.7.

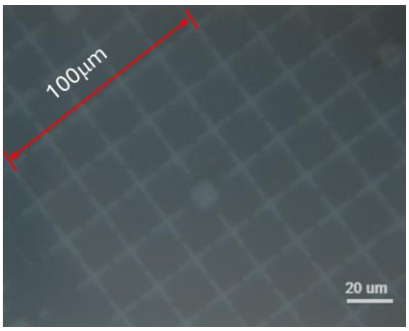

Figure 2.6. Example image of sample patterning.

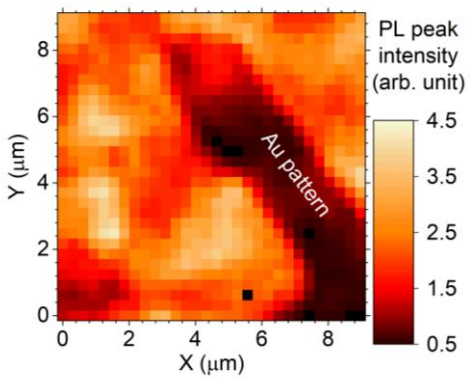

Figure 2.7. Examples of the PL peak intensity of $Ga_{0.95}In_{0.05}N$ with Au pattern.

2.9. Method of Phonon Transport Analysis

In this study, the phonon transport analysis by using 532 nm laser for observation region at GaN with 325 nm laser for heat generation at GaInN layer by simultaneous irradiation on the sample. Figure 2.8 clearly shows a schematic diagram of the method of phonon transport analysis. The 325 nm laser is higher energy than the band gap of $Ga_{1-x}In_xN$. It means that the laser is allowed to absorb by the $Ga_{1-x}In_xN$ layer. In contrast, the 532 nm laser has lower energy than the band gap of $Ga_{1-x}In_xN$. Therefore, the 532 nm laser allowing to pass through the $Ga_{1-x}In_xN$ layer and observe the underlayer of GaN in this measurement. Thus, the 325nm laser was used to detect the GaInN layer, while the 532 nm laser excitation was used to observe the underlayer of GaN. The phonon transport can be investigated by using two lasers systems in Raman spectroscopy. Table 2.1 shows the energy bandgap of the measurement sample and laser excitation.

Table 2.1. Measurement sample of the energy bandgap and laser excitation energy.

Sample	Bandgap energy (eV)
GaN	3.4
InN	0.6
InGaN (x=0.05)	3.2
InGaN (x=0.09)	3.0
InGaN (x= 0 → 0.17)	2.8
Laser excitation	**Energy (eV)**
532.09 nm	2.33
325.05 nm	3.81

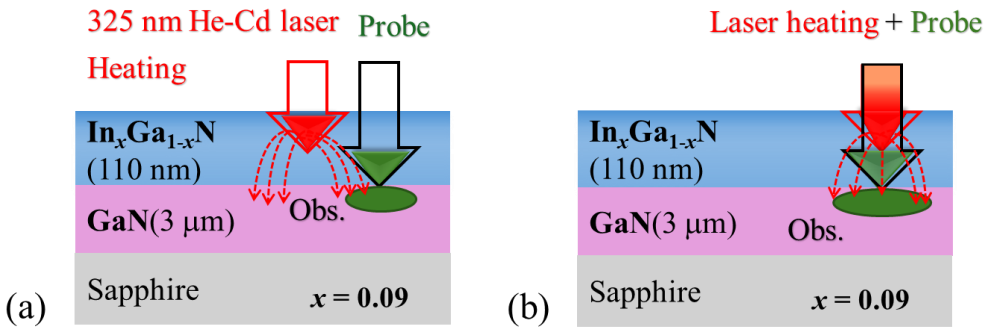

Figure 2.8. Schematic diagram of phonon transport analysis (a) $Ga_{1-x}In_xN$ (b) GaN layers.

References

[1] M. Kuball, Member, IEEE, and J. W. Pomeroy., IEEE Transactions on Device and Materials Reliability, 16(4), 667-684.

[2] M. N. Polyanskiy. Refractiveindex.info database of optical constants. Sci. Data 11, 94 (2024).

[3] J. F. Muth, J. H. Lee, I. K. Shmagin, R. M. Kolbas, H. C. Casey et al., Appl. Phys. Lett. 71, 2572 (1997).

CHAPTER 3
Methodology of PL Emission Efficiency Analysis by Integrating Raman Spectroscopy by Combination of E_2(High) and A_1(LO) Modes in a $Ga_{1-x}In_xN$/ GaN Heterostructure

Abstract

Microscopic lattice vibration images of E_2^H mode and A_1^{LO} mode or higher energy branch of LOPC modes in a GaInN film on a GaN template are obtained by using the Raman scattering spectroscopy by using the 325 nm laser. The decrease in the energy shift of E_{E2H} is obtained by increasing the temperature by increasing the laser power. The energy shift of the LOPC+ is obtained by using the theoretical formula comprising two terms based on the mode energy vibration of the bulk material and the thermal strain effect. The mapping images of the temperature and electron density in the *x*-*y* plane are simultaneously obtained by using the obtained temperature and the energy shift of the LOPC+. Finally, the image of the photoluminescence (PL) emission efficiency defined by the PL intensity per electron is obtained from the images of the PL intensity and electron density under the condition that the laser-excited electron density is higher than the residual background electron density. This method enables a quantitative discussion on microscopic photo-emission efficiency.

3.1. Introduction

Radiative carrier recombination efficiency has been discussed in many articles. Microscopic imaging of PL and cathodoluminescence (CL) are powerful measures for this purpose. The dark spots in these images exhibit the existence of threading dislocations and reveal the carrier diffusion length. However, these images are not enough to show the local radiative recombination efficiency.

When obtaining local PL using a confocal measurement system, it is considered difficult to determine the emission efficiency due to variations in carrier density caused by carrier diffusion. Although CL enables imaging of non-radiative recombination (NR) centers clustered in the vicinity of threading dislocations (TDs) when the carrier diffusion length is sufficiently short less than 500 nm [1], the luminescence peak intensity does not always show the spatial variations in emission efficiency due to the carrier diffusion or the carrier density distribution. The information of carrier density is required, and the local carrier density can be analyzed by microscopic Raman spectroscopy, where LO phonon coupling modes are analyzed.

Raman images are affected by heat energy, which is known by temperature, strain, and alloy composition. Thermal energy transport across interfaces is a critical factor in determining the accumulation of thermal energy in the active regions of electronic and photonic devices. In semiconductor films with nonuniform alloy composition, such as the GaInN system, thermal energy transport inside the film also impacts the local temperature in the active region of devices. Thermal energy transport imaging inside the thin films and across interfaces has been investigated using a microscopic Raman measurement system equipped with a double-laser setup [1,2]. For example, Raman imaging revealed the blocking of heat energy transport across the interface at misfit dislocations and TDs. However, the spatial variation of LOPC mode energies which depends on temperature, carrier density, and strain, has not been studied to investigate local carrier dynamics.

The local photoemission efficiency per electron or hole is obtained by combining the analyses of local temperature increase, LOPC, and luminescence intensity. This information can subsequently be analyzed in relation to the temperature increase resulting from NR. It will provide a deeper understanding of the interaction between recombination processes and thermal effects. The simultaneous imaging of PL intensity, carrier density, and temperature is required to provide the details of local

carrier dynamics, including both radiative and nonradiative recombination rates. The analysis of all energy modalities within the carrier–radiation–phonon system enabled to study of local carrier dynamics, especially in epitaxial films with nonuniform alloy composition and/or strain, such as GaInN. This comprehensive approach assists in understanding the interactions in materials with nonuniformity in alloy composition of nitride materials.

In this study, two-dimensional (2D) images of electron density under the photo-excitation of carriers were obtained by utilizing two phonon modes of E_{E2H} and E_{A1LO} or the higher energy branch of LOPC+ modes of a GaInN film. An image of PL efficiency as the intensity per electron is investigated, and a methodology is used to analyze the local carrier recombination processes in a nonuniform crystal field including thermal nonequilibrium carriers and phonons.

3.2. Experiment

The sample was $Ga_{0.95}In_{0.05}N$ (100 nm) / n+ -GaN (3.5 μm) / n -GaN (3 μm) heterostructure grown on an sapphire (α-Al_2O_3) substrate through a metal-organic vapor phase epitaxy process. The values of electron density (n_e) of n^+ and n -GaN were $3x10^{18}$ cm^{-3} and $1x10^{17}$ cm^{-3}, respectively. The residual electron density (n_e^0) of the $Ga_{0.95}In_{0.05}N$ layer was determined to be less than 6×10^{17} cm^{-3} by infrared (IR) reflectance analysis [1,4]. Figure 3.1 shows the reciprocal space mapping of the $(11\bar{0}5)$ X-ray diffraction and the rocking curves of the (0002) and $(101\bar{2})$ diffractions [1]. The $Ga_{0.95}In_{0.05}N$ layer was grown pseudo-morphically on the GaN template. The full-width at half maximum (FWHM) of the (0002) rocking curve was obtained to be 315 arcsecs for the GaInN layer film and 340 arcsecs for the GaN layer. The FWHM of the $(101\bar{2})$ rocking curve of the GaN layer was 486 arcsec. Assuming the TDs are generated at grain boundaries, the estimated density of screw and mixed-type dislocations was estimated to be on the order of 10^9 cm^{-2}. This estimation is consistent with the atomic force microscope (AFM) images of the GaN template wafer [1] as shown in Figure 1.1 (e).

Hook-shaped Au thin plates with a thickness of 20 nm were deposited at the four corners of every 20 μm square area aligned on the surface. Figure 3.2 shows the images of PL intensity, and the hook-shaped Au pattern images are exhibited in the PL intensity image. The Raman and PL measurement positions were identified at every

scanning measurement. However, a displacement of a few micrometers takes place in the final process to optimize the measurement conditions. Therefore, the mutual positions of the images are correlated by conducting PL measurements immediately after the Raman measurements and using the patterns of both the Raman and PL images for alignment.

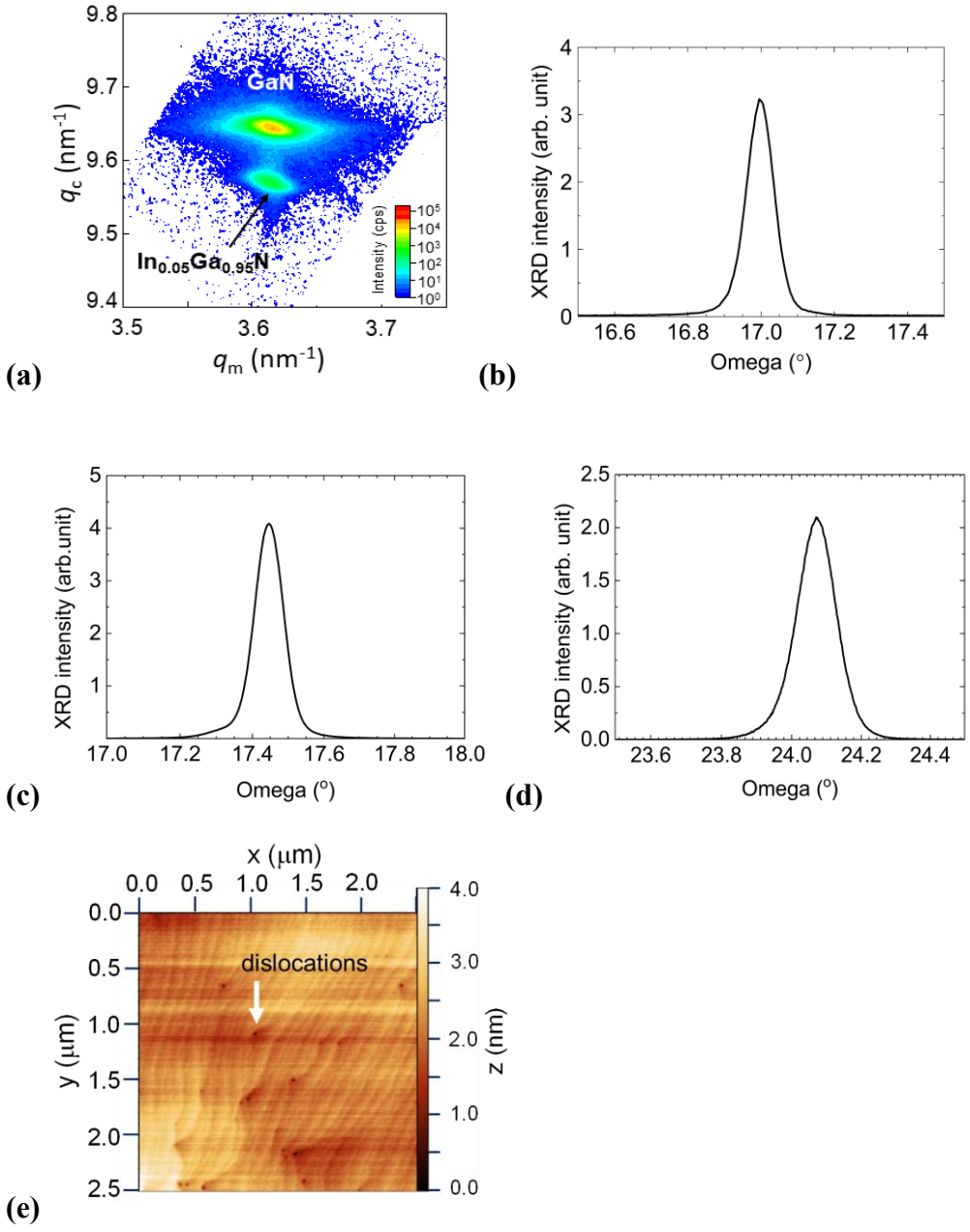

Figure 3.1. The X-ray diffraction of (a) reciprocal space mapping for $(10\bar{1}5)$, and rocking curves for (b) (0002) diffraction of the GaInN layer, (c) (0002) diffraction of the GaN layer, (d) $(10\bar{1}2)$ diffraction of the GaN layer, and AFM image of the GaN template[1].

Raman scattering and PL spectroscopies were conducted using a system equipped with a CCD camera and a monochromator with a focal length of 81 cm and a grating featuring 3600 grooves per millimeter. A 532 nm or 325 nm laser light was incident onto the sample through an objective lens with a numerical aperture (NA) of 0.47. The entrance slit of the monochromator was a cross slit, and it enabled for an in-plane resolution of 0.3 μm and also enabled confocal measurement. The microscope system was in a chamber which is maintained at a temperature of 296 (±0.05) K. The ambient temperature of the measurement system was maintained at 296 (±1) K. The relaxation energy of an excited electron-hole pair to the band bottom is estimated to be 16.6 (±1.3) % of the excitation photon energy which was obtained from the energy difference between the excitation laser and the PL peak. The PL peak energy is thought to represent the final energy states of electrons and holes before photoemission. This energy is considered to be determined by the local energy states in the nonuniform energy structure, and it was not determined by the average bandgap energy in the GaInN crystal. Additionally, further energy is expected to be transferred to the lattice vibration system through NR processes. Raman images in the *x*-*y* plane were obtained for the E_2^H and A_1^{LO} or LOPC+ modes. PL imaging was conducted using the same optical system as the Raman imaging with the surrounding temperature at 296 K.

3.3. PL Imaging on Sample Surface

The investigation of the images of PL peak energy and intensity measured at a laser power of 0.1 mW on the sample surface are shown in Figure 3.2. Since the excitation laser light and the PL partially transmit through the Au film of the pattern, the PL peak energy image can be captured across the entire region. A hook-shaped Au pattern can be observed where the PL intensity is weak. Raman imaging was conducted in the square regions. In the vicinity of position ①, the PL peak energy is lower than that of the surrounding region, which reveals that the energy gap (E_g) in this region is higher InN mole fraction. This feature suggests that carriers are expected to be localized because of the lower carrier-escape probability due to the potential barrier of 20 – 25 meV. In this region, PL intensity is lower than that of the surrounding region. Thus, it is considered that the PL emission efficiency is required to be investigate to know the information of local carrier density. Figure 3.3 expresses the spatial nonuniformity of

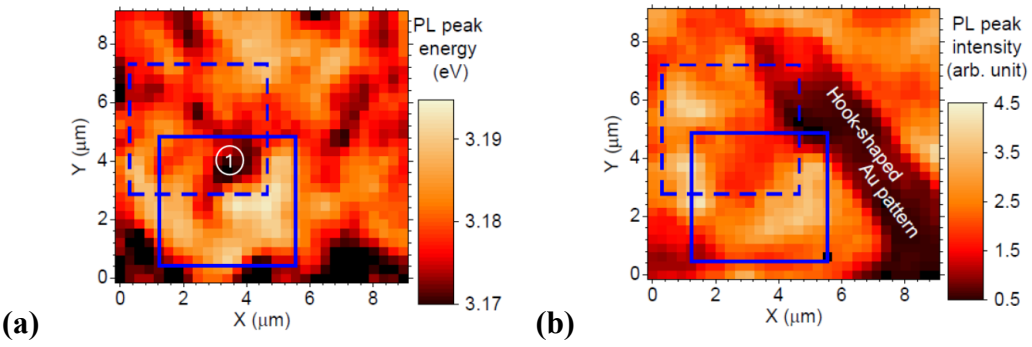

Figure 3.2. PL imaging of (a) peak energy, and (b) intensity of the $Ga_{0.95}In_{0.05}N$ layer by the 325 nm excitation. Note that Raman measurements were conducted inside the square regions.

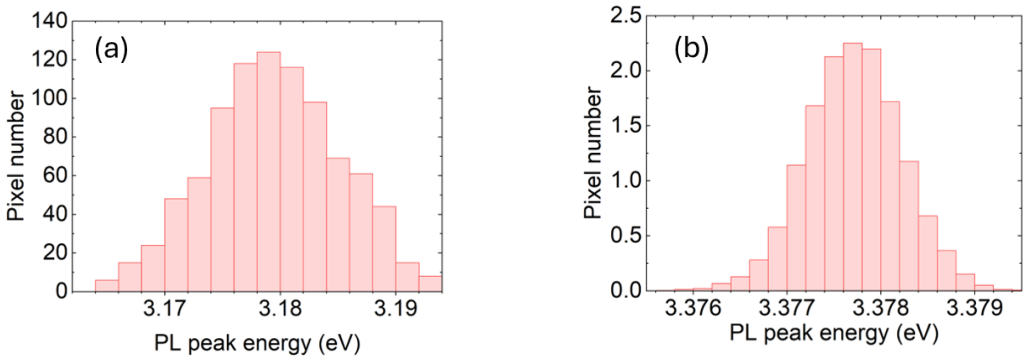

Figure 3.3. The histograms of the distribution of PL peak energies for (a) the GaInN layer and (b) the GaN layer.

the peak energy variation in GaInN and GaN layers of the energy states of approximately 20–25 meV for GaInN and 2 meV for the underlayer of GaN.

Figure 3.4 illustrates an example of PL intensity as a function of the distance between the excitation and observation positions and the decay of PL intensity in a time-resolved photoluminescence (TRPL) measurement. Figure 3.4 (a), (b), and (c) show the *x*-*y* mapping images of PL intensity, peak energy, and FWHM respectively. The PL intensity is investigated on the three lines with keeping the exctitation position at the right side edge of these lines even if the observation position is shifted from the excitation position by several micrometers, the PL is observed. The candidate reasons of this luminescence diffusion include carrier diffusion, multiple cycles of absorption and emission, as well as the waveguide effect of the GaInN layer. When considering the increase in the absorption coefficient with increasing photon energy, the PL peak

energy is expected to shift to the lower energy side by radiation traveling inside the GaInN film. However, the PL peak energy did not exhibit a shift to the lower energy side as shown in Figure 3.5. It indicates that the transport of luminescence due to the waveguide effect of the GaN layer is excluded from the candidate origins. The possible reasons are carrier diffusion and repeated absorption and emission. It is thought that the latter process also extends the volume of carrier existence. Figure 3.4 (d) indicates that the effective carrier diffusion length is thought to be in the range of 1.5–2.5 μm. The TRPL measurement was conducted using 266 nm laser pulses with a pulse duration of 150 fs and a repetition frequency of 80 MHz, a high-speed photomultiplier, and a time-correlated single photon counting system. The PL lifetime was observed to be approximately 80 ps, as shown in Figure 3.6. These results suggest that the carrier density in the $Ga_{0.95}In_{0.05}N$ layer is in the order of 10^{17} cm^{-3} for an excitation power of 1 mW of the 325 nm laser in the present microscopic system, assuming the complete absorption of the incident laser light in the $Ga_{0.95}In_{0.05}N$ layer and the uniform confinement of carriers in the layer.

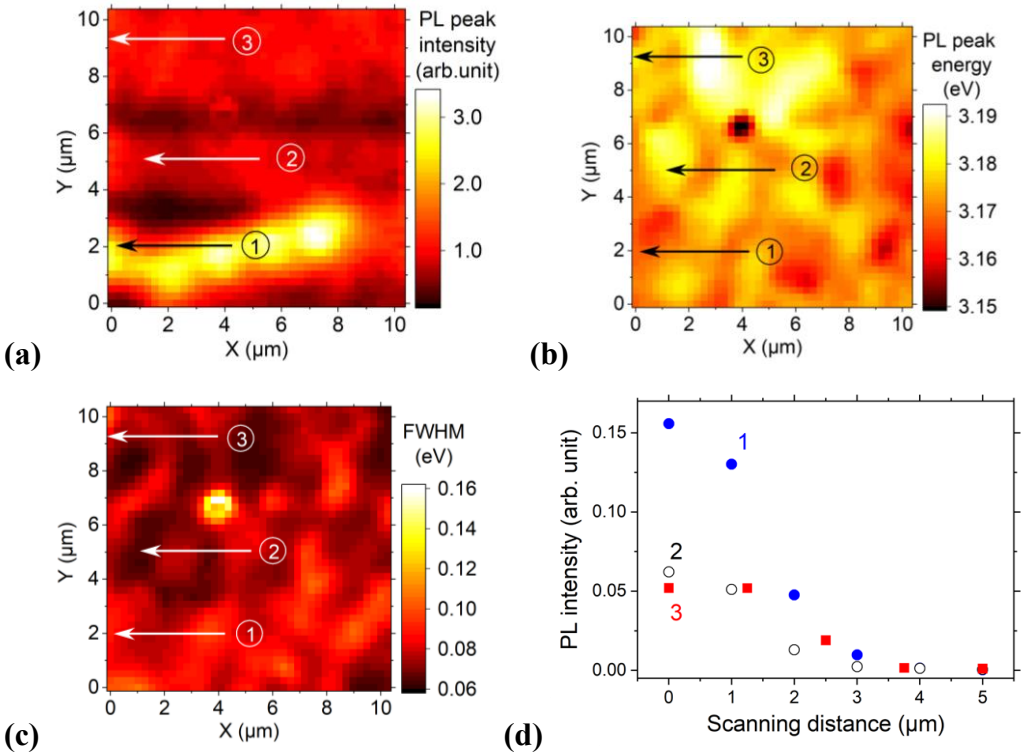

Figure 3.4. PL imaging includes the three measurement scan lines: (a) intensity, (b) peak energy, (c) FWHM, and (d) PL imaging as a function of the distance between the excitation and observation positions.

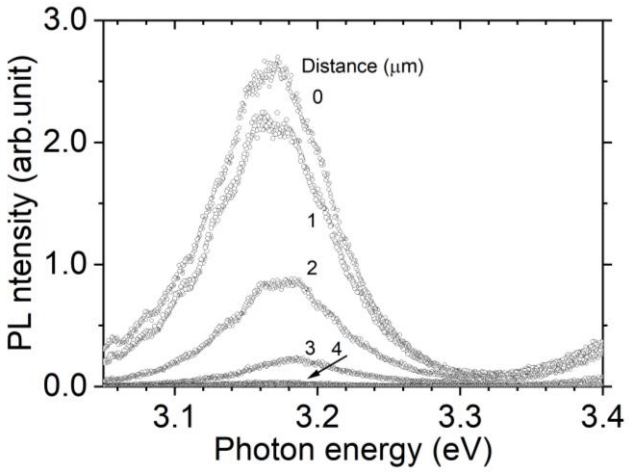

Figure 3.5. Example of PL spectrum as a function of the distance between the excitation position and observation position. Note that the position is from line (1) in Figure 3.4.

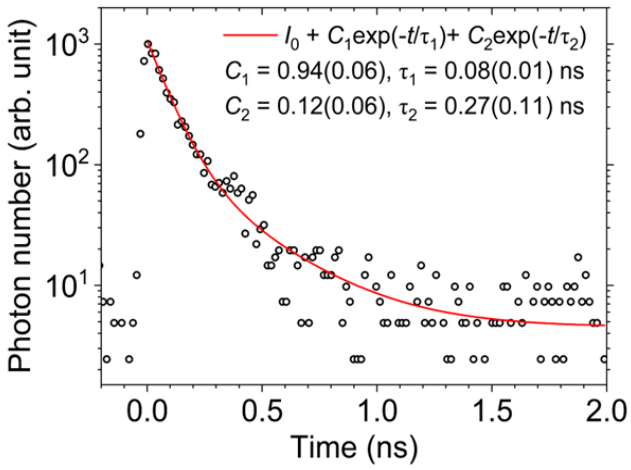

Figure 3.6. PL lifetime for $Ga_{0.95}In_{0.05}N$.

3.4. Temperature development of PL intensity by the laser excitation

Figure 3.7 describes an example of Raman scattering spectra obtained using the 325 and 532nm lasers. The figure highlights the difference in the peak energies of E_2^H and A_1^{LO} modes between the two excitation laser wavelengths. This variation is attributed to the short penetration depth of the 325 nm light (70 nm depth) caused by absorption from the interband transition in the $Ga_{0.95}In_{0.05}N$ film. The beam waist length in the depth direction is calculated to be 4.7 μm, and it indicates that the Raman signals mainly represent the properties of the surface 70 nm region of the penetration depth.

For the 532 nm laser, which is not absorbed in the GaInN layer, the beam waist length in the depth direction is estimated to be 7.8 μm. Since the focus point was adjusted to the sample surface during the observation, the upper 3.9 μm region of the 6.5 μm thick GaN layer was primarily observed. The contribution of the 100 nm thick GaInN layer to the Raman signal is significantly limited when using the 532 nm laser. The peak energies of these modes shift to the lower energy side by increasing the excitation power as shown in Figure 3.7 (b). This shift reflects the temperature increase caused by the rising amount of relaxation energy from the excited carriers.

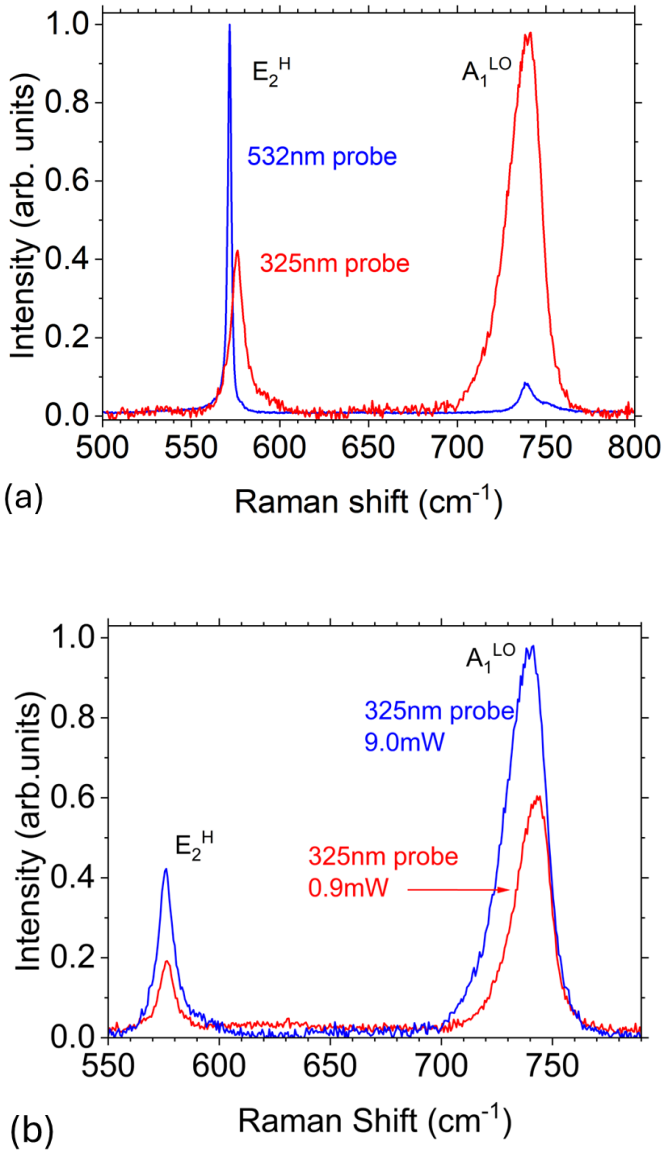

Figure 3.7. Raman scattering spectra (a) using 532 nm and 325 nm laser, and (b) 325 nm with two different laser powers.

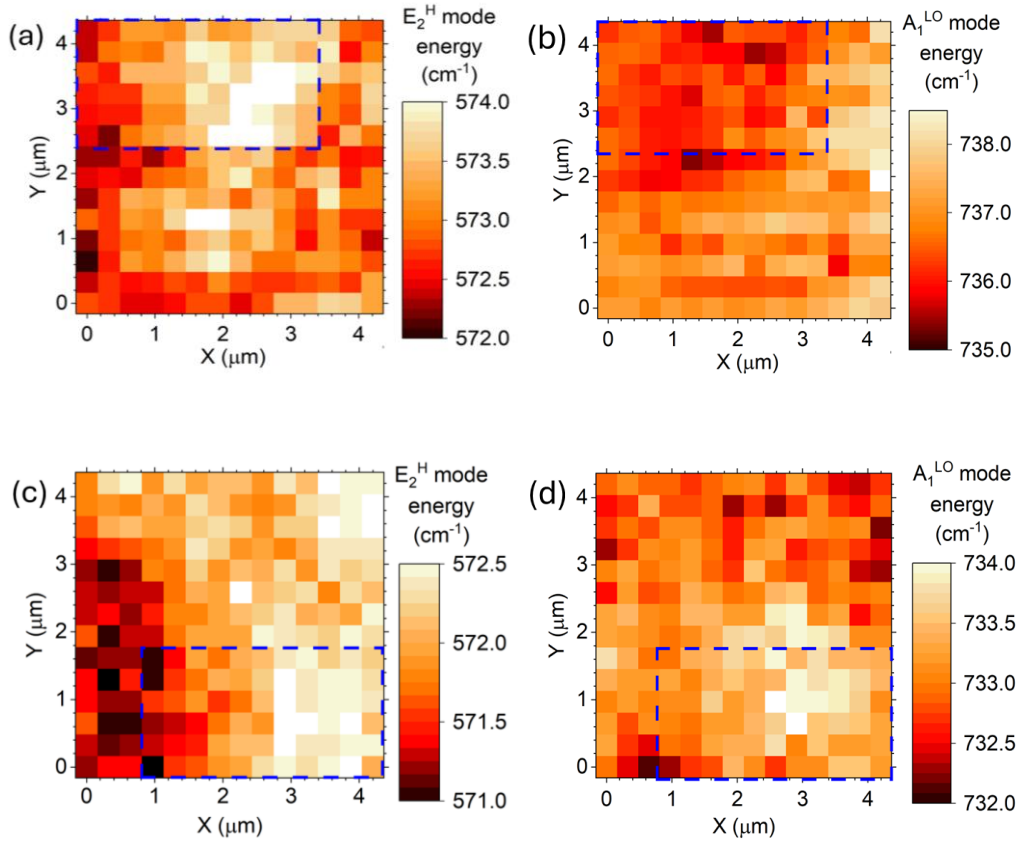

Figure 3.8. Mapping images of E_{E2H} with 325 nm laser excitation in (a) and (c) at 0.7 mW laser power, and E_{A1LO} in (b) and (d) at 9.0 mW laser power. Note that the dashed line squares show the same measurement region.

Figure 3.8 shows the E_{E2H} and E_{A1LO} spectrum peak energies at excitation powers of 0.7 mW and 9.0 mW. The regions inside the squares are consistent in the measurements of the two excitation powers. The energy shift to the lower energy side, $\Delta E_j(\Delta T)$ suggests an increase in temperature (ΔT). $\Delta E_j(\Delta T)$ can be approximately expressed by two terms which is the energy shift of bulk material with a uniform temperature $(\hbar\partial\omega_j/\partial T)\,.\Delta T$, and the shift caused by thermal strain Equation (3.1).

$$-\Delta E_j(\Delta T) = \frac{\hbar\partial\omega_j}{\partial T}\Delta T - \left(2a_j - 2b_j\frac{v}{1-v}\right) l_{th\parallel}\,\Delta T \qquad (3.1)$$

where, a_j, b_j, v, and $l_{th\parallel}$ are compressive and shear deformation potentials of the modes of E_2^H (j = E2H) and A_1^{LO} (j = A1LO), Poisson ratio, and linear expansion coefficient in c plane, respectively. E_j is $\hbar\omega_j$. Table 3.1 shows reference parameters for GaN and InN. In this study, two values of $\partial E_j/\partial T$ for InN were calculated based on the

reported ΔE_j values obtained from samples on sapphire substrates. In addition, the difference in $l_{th\parallel}$ between InN and α-Al_2O_3 was taken into account for the thermal strain in the InN film. The data of $\partial E_j/\partial T$ for InN were obtained from the free-standing InN films produced via molecular beam epitaxy (MBE) growth. The parameters for $Ga_{0.95}In_{0.05}N$ were obtained by linear interpolation between the values of GaN and InN.

Table 3.1 Parameters utilized in the calculation.

	a	b	ω_j	$\partial\omega_j/\partial T$	v	$l_{th\parallel}$
	cm^{-1}	cm^{-1}	cm^{-1}	$10^{-2}\,cm^{-1}K^{-1}$		$10^{-6}\,K^{-1}$
E_{E2H}						
GaN	-742[3]	-715[3]	567.6 [7]	-1.5	0.183	5.7 [8]
				[a](300~500 K)	[18]	(573 K)
	-1027[9]	-597[9]	567.9 [9]	-1.7 [b]		4.2[8]
						(296 K)
	-850[10]	-920[10]	568.4 [3]	-2.2 [12]	0.21 [6]	4.0 [5]
	-911[11]	-852[11]		-6.2 [14]		
InN	-938[6]	-407[6]	494.6 [6]	-4.8[b]		
	-610[13]	-857[13]				
E_{A1LO}						
GaN	-664	-881	736.4[3]	-2.4 [18]		
	-685	-997		-3.7[b]		
InN	-901	-587	582.3[6]	-3.3[c]		
				-11[d]		
				-8.2[b]		

(a)Average between 300 and 500 K in ref [18]. (b) present work (280-380 K). (c) calculated from ref [12]. (d) calculated from ref [14]. $\partial\omega_j/\partial T$ shows the mode energy derived from bulk material with a uniform temperature.

Figure 3.9 shows the decrements in the mode energies in the common measurement area inside the dashed squares in Figure 3.6. Figure 3.9 (c) shows that the ratio of $\Delta E_{A1LO}/\Delta E_{E2H}$ is in a region of 1 to 3.6. Figure 3.10 expresses the uncertainty of these mode energies. The uncertainty is mostly less than 0.25 cm^{-1}, while values up

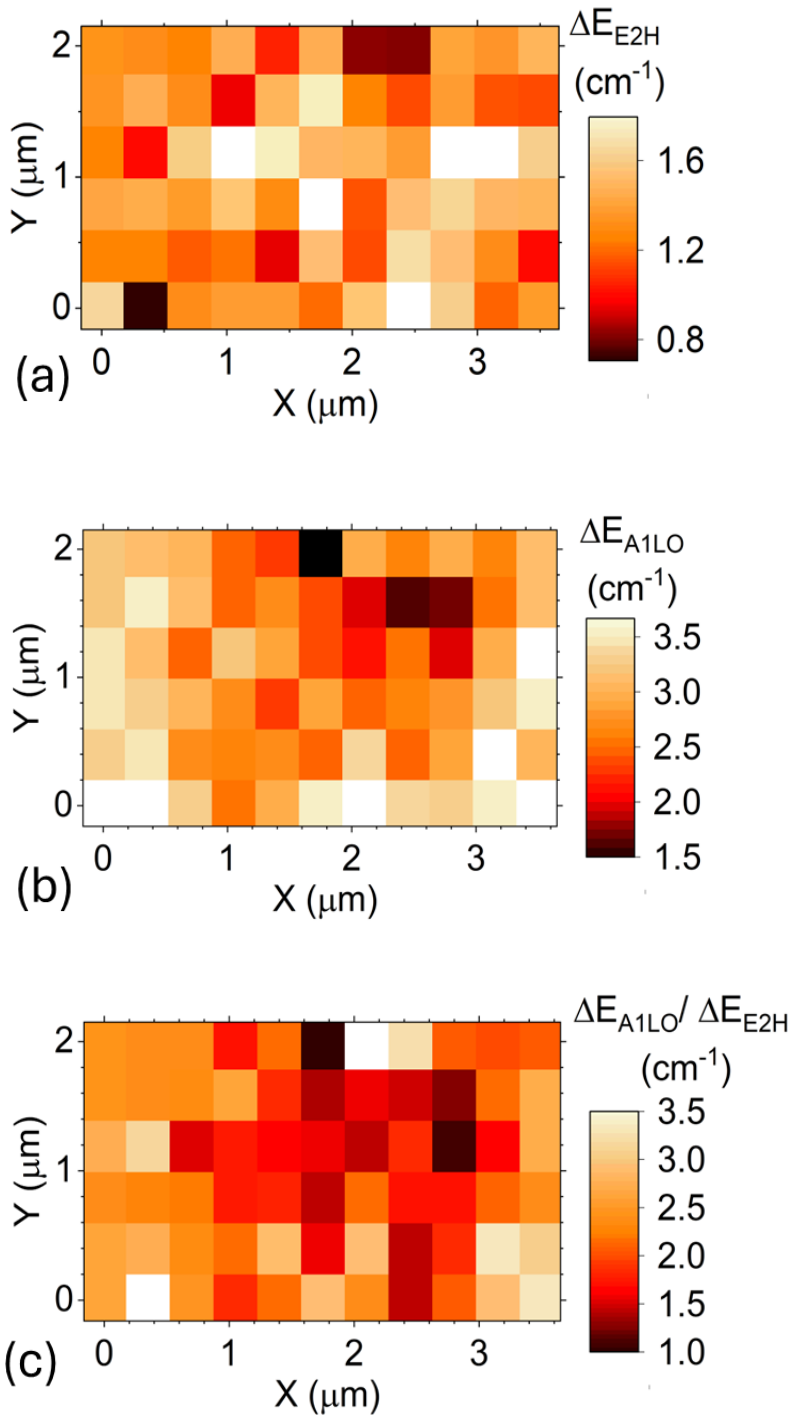

Figure 3.9. Mode energy decrements in (a) E_{E2H} and (b) E_{A1LO} by increasing the 325 nm laser power from 0.7 mW to 9.0 mW and (c) the ratio of these energy decrements.

to 0.4 cm^{-1} are observed in some regions. These images reveal the validity of the observed spatial nonuniformity in the images of ΔE_{E2H} and ΔE_{A1LO}. The ratio of $\Delta E_{A1LO}/\Delta E_{E2H}$ is lower in the center region. This ratio, covering a range of 1 to 3.6, is

attributed to the nonuniform increase in n_e, which is higher in the regions with a higher InN mole fraction.

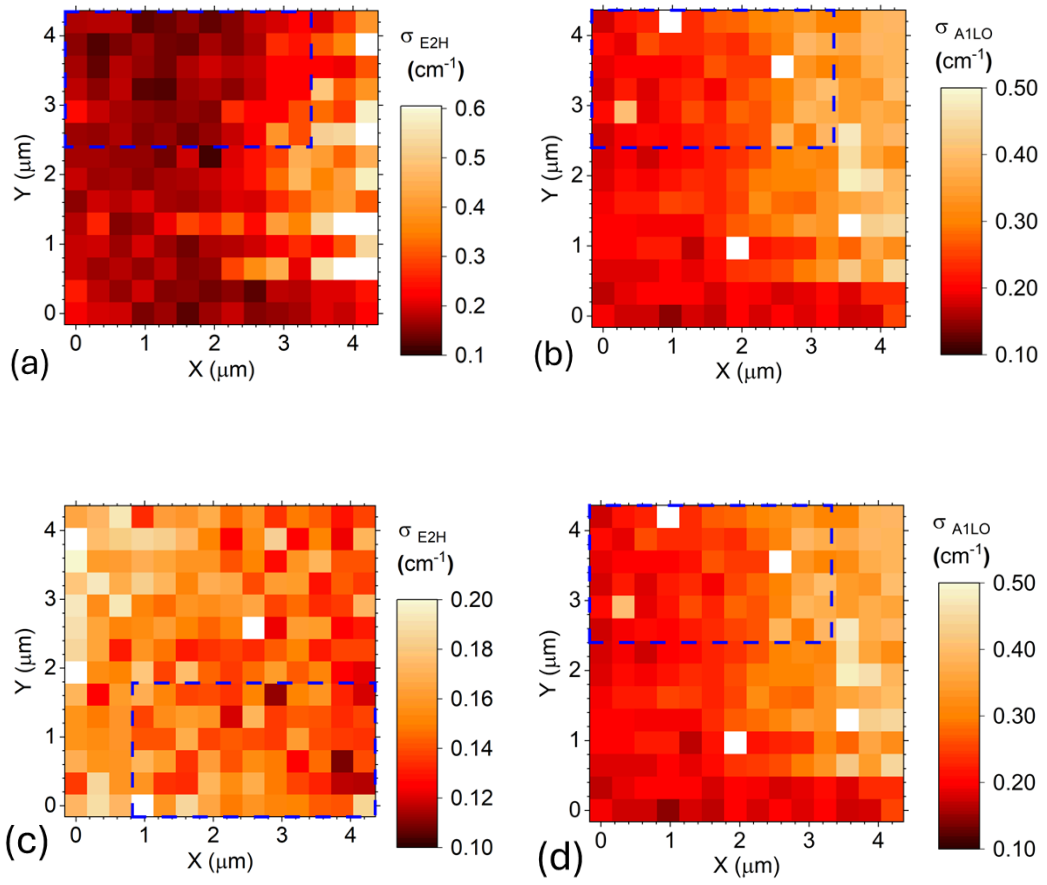

Figure 3.10. Images of uncertainty values of E_{E2H} with 325 nm laser excitation in (a) and (c) at 0.7 mW laser power, and E_{A1LO} in (b) and (d) at 9.0 mW laser power.

When observing the temperature increase in the n-GaN layer using double lasers of 532 nm for probing and 325 nm for heating the GaInN [1], ΔE_{E2H} of the n-GaN layer was observed with a decrease to approximately 10% of the value observed in the GaInN layer. Additionally, it was further reduced by 60% when the probing position was moved 20 μm laterally from the excitation point. The energy of the Raman peak at 414 cm^{-1} from the sapphire substrate remained constant within an error of 0.03 cm^{-1} at a position 5 μm away from the excitation point, indicating that the temperature increase deep within the sapphire substrate is negligible. Thus, the assumption of the thermal strain model in Equation (3.1) is valid. As shown in Table 3.1, several deformation potential values have been reported for GaN. Regarding the Poisson ratio, values of

0.183 for GaN and 0.21 for InN were adopted. In the study, the validity of these deformation potential values is expressed.

3.5. Analysis of Temperature and Electron Density

Figures 3.2 and 3.8 indicate that the E_{E2H} is mostly higher in the region of lower PL peak energy. This result indicates that E_{E2H} is higher in regions with a higher InN mole fraction, where the increase in E_{E2H} by the compressive strain dominates. A mode energy E_j(j = E_2^H or A_1^{LO}) is expressed in Equation (3.2) as a function of InN mole fraction of x.

$$E_j(x) = E_j(0)\,(1-x) + E_j(1)\,x + \left(2a_j - 2b_j\,\frac{v}{1-v}\right)\frac{x(\alpha_0-\alpha_1)}{\alpha_1 x + \alpha_0(1-x)} \quad (3.2)$$

where α_0 and α_1 are the a lattice constants of GaN and InN, respectively. Here, a linear dependence of mode energies on the mole fraction of x is assumed. The respective a lattice constants of GaN and InN of 3.189 Å and 3.548 Å are utilized in this study. The nonuniformity of E_2^H corresponds to an alloy composition fluctuation of 0.007 where measured value of fluctuation is 1.5 cm^{-1} in Figure 3.8 (a). This value agrees with the fluctuation value obtained from the PL peak distribution of 25 meV when assuming the bowing factor of 0.7 eV [22].

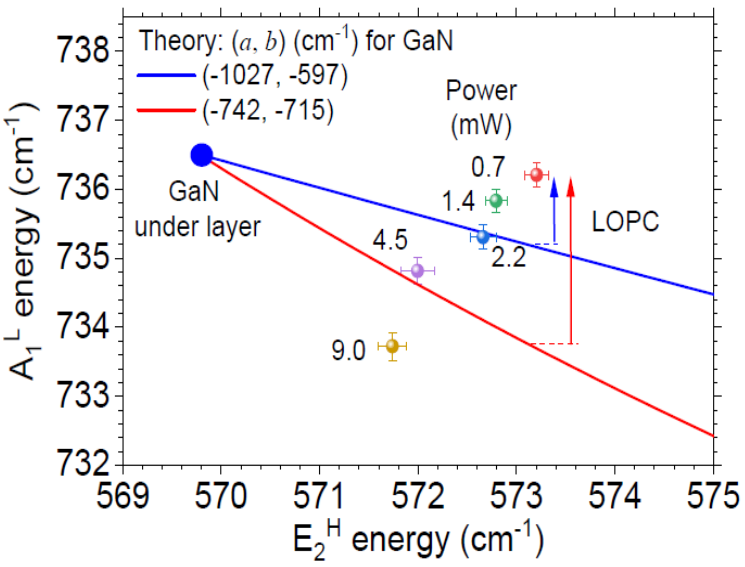

Figure 3.11. Relation of E_2^H and A_1^{LO} energies of the pseudo-morphologically grown $Ga_{0.95}In_{0.05}N$/GaN. Note that the numbers in the figure show the excitation power in the unit of mW and the solid lines are the theoretical functions.

Figure 3.11 exhibits an example of the experimental relation between E_2^H and A_1^{LO} peak energies and theoretical functions. Two examples of theoretical functions are plotted in Figure 3.10. The adopted values of the deformation potential values for A_1^{LO} are a= -664 cm^{-1} and b = -882 cm^{-1} for GaN, and a = -901 cm^{-1} and b= -587 cm^{-1} for InN. For E_2^H , a = -938 cm^{-1} and b= -407 cm^{-1} for InN are adopted, and these values are utilized in these fixed functions. Two sets of deformation values of a and b of E_2^H for GaN are (-1027, -597) cm^{-1} and (-742, -715) cm^{-1} are adopted. Here, the Poisson ratio of 0.183 for GaN is adopted. The two listed data sets for A_1^{LO} in GaN give 10% difference in dE_{A1LO}/dT for the GaInN layer. Thus, the values of (-664, -881) cm^{-1} for A_1^{LO} in GaN are selected. For InN, the adopted data set for both E_2^H and A_1^{LO} was obtained from an experiment [29]. The plot of the energy pair (E_2^H, A_1^{LO}) at 0.7 mW excitation power is located above both the theoretical functions in Figure 3.11. This relation is attributed to the shift of the LOPC+ energy from the pure E_{A1LO}, which excludes the effect of the plasmon. Since the GaN layer on the α-Al_2O_3 substrate is strained, the theoretical curve obtained using Equation (3.2) is shifted parallelly. Thus, the point at x = 0 agrees with the experimentally obtained (E_2^H, A_1^{LO}) of the GaN underlayer as an approximation.

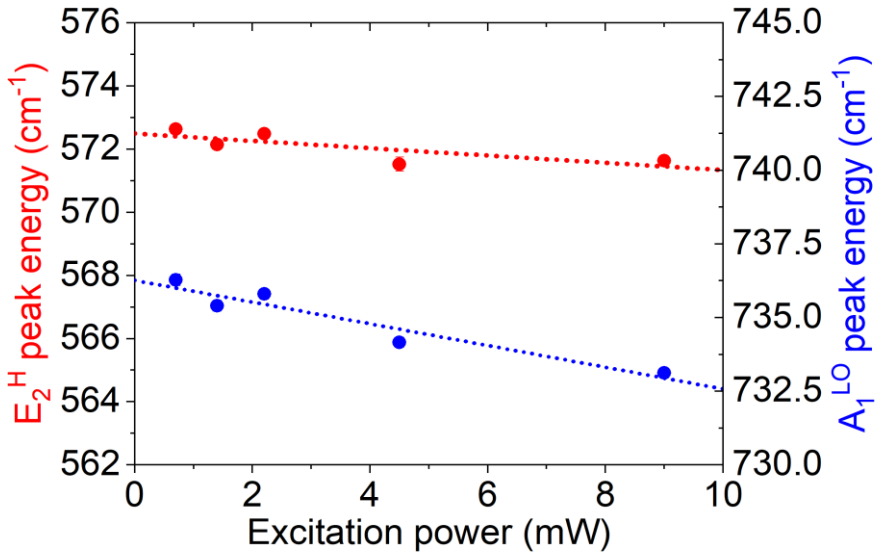

Figure 3.12. The value of E_2^H and A_1^{LO} modes in the $Ga_{0.95}In_{0.05}N$ layer as a function of excitation laser power.

Figure 3.12 shows an example of the E_2^H and A_1^{LO} peak energies as a function of the excitation laser power. Using the intersection of E_2^H energy at 0 mW and the

theoretical relation shown in Figure 8, the A_1^{LO} peak energy at zero-laser power limit was obtained. The difference between the A_1^{LO} peak energy at the zero-power limit and the value obtained by the theoretical relation using Equation (2) is attributed to the energy increase of the LOPC+ mode, and it is represented by the pure A_1^{LO} energy without the plasmon effect compared to the A_1^{LO}. The LOPC+ mode energy $E+$ was obtained using Equation 3.3(a).

$$E_+^2 = [E_P^2 + E_{A1LO}^2 + \sqrt{(E_P^2 + E_{A1LO}^2)^2 - 4E_P^2 E_{A1TO}^2}]/2 \quad (3.3\ a)$$

$$E_P = \hbar\sqrt{(n_e e^2/m_\parallel \varepsilon_\parallel(\infty)} \quad (3.3\ b)$$

$$E_{A1TO}\ /E_{A1TO} = \sqrt{\varepsilon_\parallel(\infty)\ /\varepsilon_\parallel(0)} \quad (3.4)$$

where, E_{A1LO}, E_P, $\varepsilon_\parallel(\infty)$, and $m_\parallel$ are represented as A_1(TO) (A_1^{TO}) phonon mode energy, plasmon energy, the dielectric constant at the high-frequency limit, and effective electron mass, respectively.

The values of $\varepsilon_\parallel(\infty)/\varepsilon_0$ and $m_\parallel/m_0$ are obtained from the linear interpolation of the values of GaN and InN. The ε_0 and $m_0$are the dielectric constant of the vacuum and electron rest mass, respectively. Table 2 shows the parameters for GaN and InN. $\varepsilon_\parallel(0)$ was obtained from the relation of Equation (3.4).

Table 3.2. Parameters required for the discussion on LOPC. $\varepsilon_\parallel(\infty)/\varepsilon_0$ of InN was obtained form E_{A1LO} =582.3 cm^{-1} and E_{A1LO} 449.0 cm^{-1} and $\varepsilon_\parallel(0)/\varepsilon_0$ = 7.0 [15] of InN using the Lyddane-Sachs-Teller relation.

	$\varepsilon_\parallel(\infty)/\varepsilon_0$	$\varepsilon_\parallel(0)/\varepsilon_0$	m/m_0
GaN	5.01[16]	9.14 [16]	0.24[17]
InN	7.0[15]	11.7	0.054 [15]

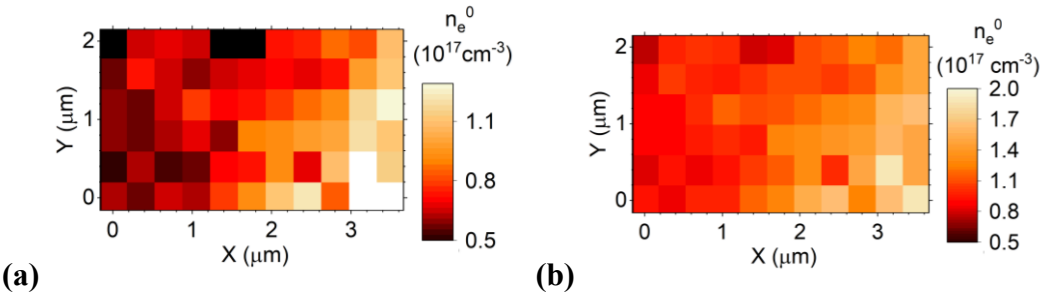

Figure 3.13. Residual carrier density n_e^0 for the conditions of (a) (a,b)= (-1027,-597) for GaN, and (b) (a,b) = (-742,-715) for GaN.

Since the coupling with the hole plasmon is negligible due to the high scattering rate and heavy hole mass [30,31], the observed shift is attributed to coupling with the electron plasmon. The obtained mapping of the residual electron density n_e^0 is shown in Figure 3.13. It was found that the deformation potentials listed in Table 3.1 give a residual electron density n_e^0 in the range of less than 6×10^{17} cm^{-3} from the IR reflectance analysis.

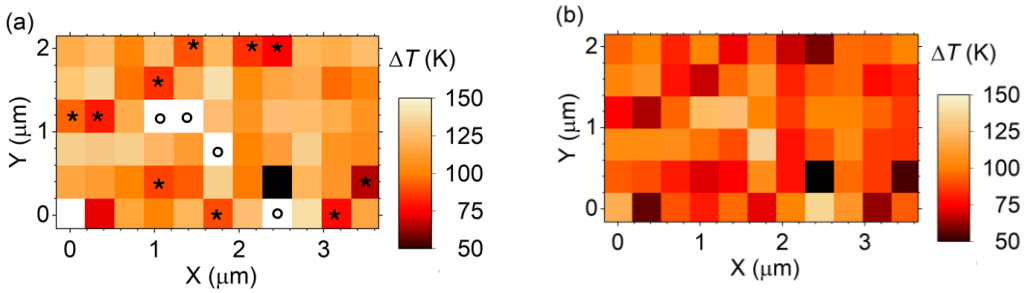

Figure 3.14. Examples of images of temperature increase in the $Ga_{0.95}In_{0.05}N$ layer obtained from ΔE_{E2H} (a) $(a,b) = (-1027,-597)$ for GaN, and (b) $(a,b) = (-742,-715)$ for GaN.

When adopting the value of $(a,b) = (-1027,-597)$ of GaN for the theoretical curve in Figure 3.11, the temperature-dependent variations of the phonon mode energies of the $Ga_{0.95}In_{0.05}N$ layer are expressed in cm^{-1}. These variations are calculated using the thermal expansion coefficient values of GaN at the two listed temperatures.

$$E_{E2H}(T) = -\int_{296}^{T}(1.39 - 9.24\times10^{-4}T)\times10^{-2}dT \qquad (3.5\text{ a})$$

$$E_{A1LO}(T) = -\int_{296}^{T}(3.67 - 4.95 \times 10^{-4}T) \times 10^{-2}dT \quad (3.5\ b)$$

where, the base temperature of 296 K, used in Raman measurements, is adopted for the calculations of temperature-dependent variations in the phonon mode energies of the $Ga_{0.95}In_{0.05}N$ layer. When exciting the sample with a 9 mW laser, the temperature increase ΔT was determined from ΔE_{E2H} due to the power increase from 0 to 9 mW. Two examples of using $(a, b) = (-1027, -597)$ and $(-742, -715)$ for GaN, are plotted in Figure 3.14. The highest temperature increase in the center region is 150K and for Figure 3.14(a) and 120K for Figure 2.14(b).

Equation (3.5) provides the ratio of $\Delta E_{A1LO}(T)/\Delta E_{E2H}(T)$ in the range of 3.6 ~ 4.2 in the temperature range of 450 ~ 545 K. The maximum value observed in the experimental results of Figure 3.9 (b) is consistent with this theoretical estimation. The distribution of this ratio to lower values is attributed to the variation in LOPC+ energy due to the variation in the increase in n_e by increasing the laser power.

Using the temperature T obtained from Equation (3.5 a) and (3.5 b), the E_{A1LO} value free from the LOPC+ effect at 9 mW excitation was obtained. This value was found to be lower than the experimentally obtained E_{A1LO} or LOPC+ energy, which is attributed to the increase in n_e by laser irradiation. Figure 3.15 schematically shows the relation between the experimentally and theoretically obtained E_{A1LO} or LOPC+ energy. Figure 3.16 shows the histogram of the effective increase in the E_{A1LO} or LOPC+ energy shift due to the excitation laser irradiation (ΔE_{LOPC}) for the two deformation potential data sets for E_2^H of GaN at $(a, b) = (-1027, -597)$, $(-911, -852)$, and $(-742, -715)$.This figure indicates the inclusion of negative ΔE_{LOPC} or the decrease in n_e due to laser irradiating, particularly in the case of Figure 3.16 (b). This contradiction is attributed to the uncertainty of the mode energies as shown in Figure 3.10. The uncertainty values at positions 1 and 2 in Figure 3.9 (c) are listed in Table 3.3. As $\Delta E_{A1LO}(T)/\Delta E_{E2H}(T)$ calculated using Equation (3.5) covers within the range of 3.6 to 4.2, the uncertainty of 0.24 cm^{-1} and 0.38 cm^{-1} for E_{E2H} corresponds to the error up to 1.1 and 1.6 cm^{-1} for E_{A1LO}. Therefore, the negative values of 1.7 cm^{-1} in Figure 3.16 (b) and (c) are considered acceptable within this uncertainty range. ΔE_{LOPC} is plotted in Figure 3.17 (a) and (b) for the two (a, b) pairs of GaN for $(-1027, -597)$ and $(-742, -715)$. In the latter case, in the right side region of x at 3.4 to 3.6 μm, the image is dominated by negative values. It is thought to be beyond the statistical

randomness of the appearance of negative values under the condition of the E_{A1LO} uncertainty of 1.6 cm^{-1}. In the case of the (a, b) of $(-911, -852)$and $(-742, -715)$, ΔE_{LOPC} are negative in 25% and 47% of the measured region. Finally, it is found that the deformation potentials (a, b) of $(-1027, -597)$ is acceptable with respect to ΔE_{LOPC}.

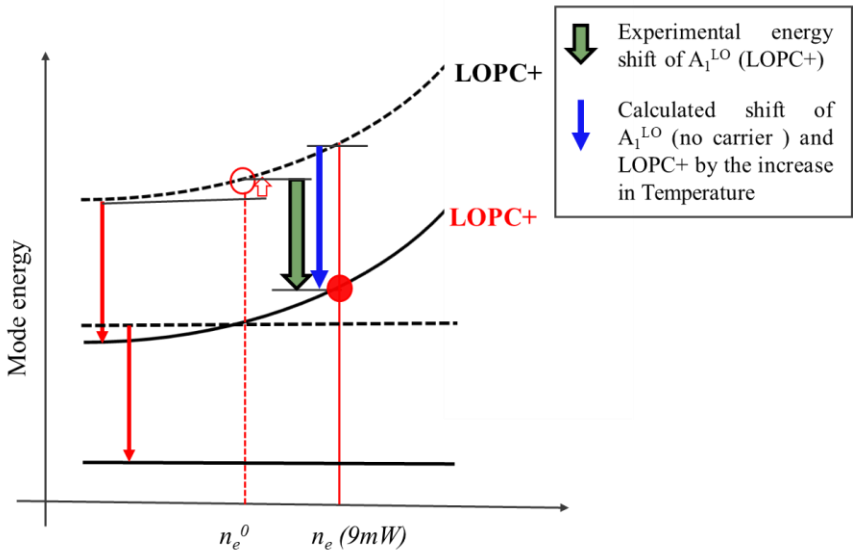

Figure 3.15. Schematic of the relation among of the shift values experimentally obtained E_{A1LO} including the effect of the LOPC and pure A_1^{LO} excluding the effect of the LOPC.

Table 3.3. Uncertainty values of phonon mode energies in the mapping images.

Position	E_{E2H} (cm^{-1})			E_{A1LO} (cm^{-1})		
	Power (mW)		ΔE_{E2H}	Power (mW)		ΔE_{E2H}
	0.7	9.0	-	0.7	9.0	-
1	0.29	0.19	0.38	0.25	0.39	0.46
2	0.17	0.17	0.24	0.18	0.17	0.24

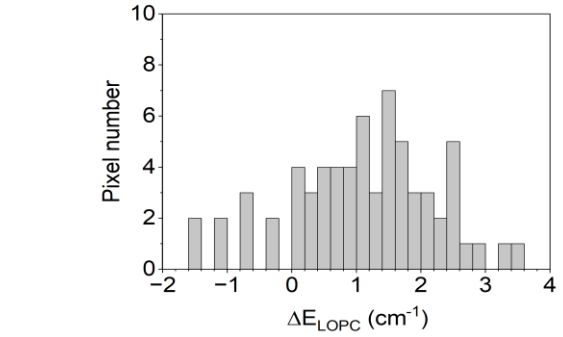

(a)

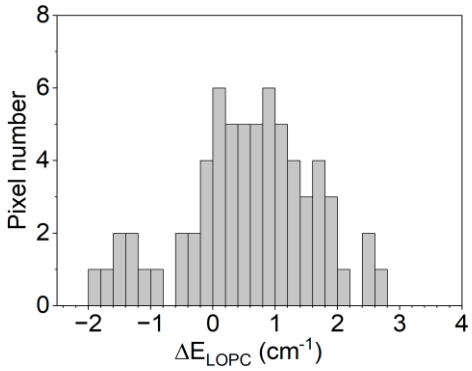

(b)

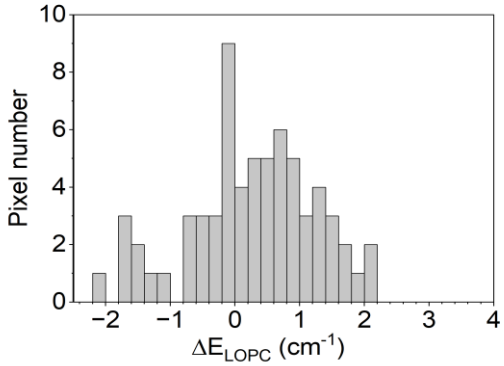

(c)

Figure 3.16. Histogram of effective LOPC+ energy shift by irradiating the 9.0 mW laser (a) $(a, b) = (-1027, -597)$ (b) $(a, b) = (-911, -852)$, and (c) $(a, b) = (-742, -715)$ for GaN. Note that the negative value occupies 10%, 25% and 40% of pixels in the images of ΔE_{LOPC} for (a), (b), and (c), respectively.

The images of n_e obtained by the present process based on the LOPC+ mode energy at 9 mW excitation power with (a, b) of $(-1027, -597)$ for GaN are exhibited in Figure 3.17 (c). Electron density up to 2 x10^{17} cm^{-3} is obtained. It is found that the n_e at 9 mW excitation power is consistent for the (a, b) of $(-1027, -597)$. In this figure,

a high n_e is observed in the region of high InN mole fraction region where the high E_{E2H} is obtained. However, the PL intensity in this region is lower than in the surrounding region, as demonstrated in Figure 3.2 (b). Figure 3.16 (d) represents the PL intensity per electron, indicating low emission efficiency in the region of high electron density shown in Figure 3.17 (c). The result reveals a higher nonradiative recombination or a lower radiative recombination rate in the high n_e region. Figure 3.14 shows a higher increase in temperature in the centre regions, it indicates a higher nonradiative recombination rate in that region, while the emission efficiency is not so low. However, the highe carrier injection rate and high nonoradiative recombination rate possibly affects.

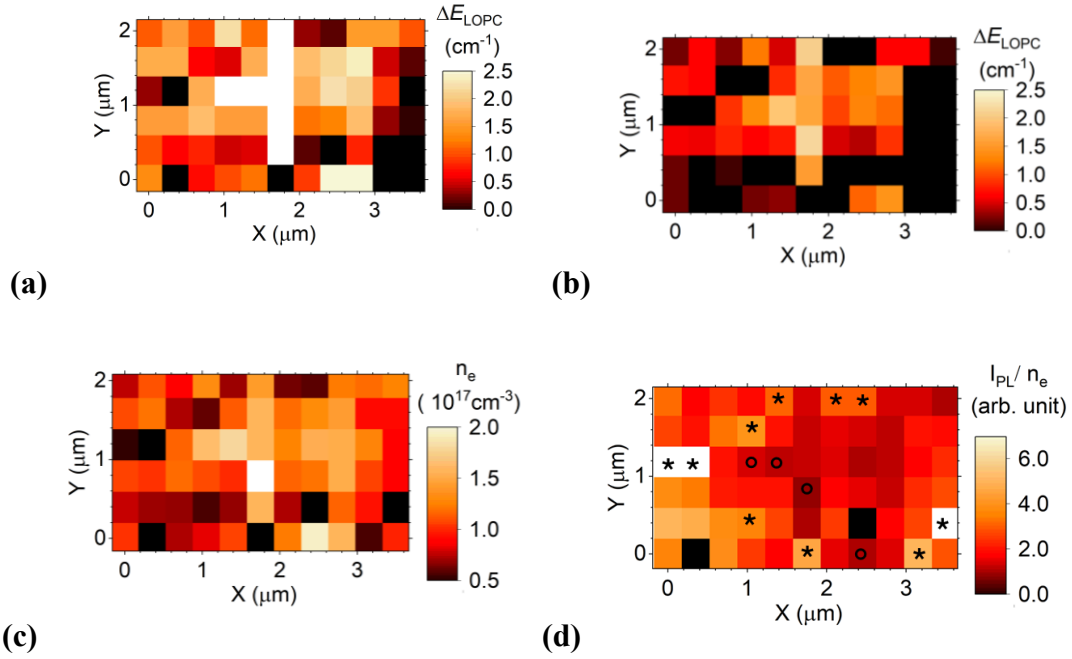

Figure 3.17. Images of ΔE_{LOPC} for two (a, b) pairs of GaN (a)$(-1027, -597)$ (b) $(a, b) = (-742, -715)$ (c) n_e at 9 mW excitation for $(a, b) = (-1027, -597)$ for GaN (d) PL emission efficiency for the case of (c).

3.6. Conclusion

The temperature increases were detected by the analysis of E_{E2H}, and E_{A1LO} can be extracted without the influence of LOPC+ effects in this study. Differences between E_{A1LO} and LOPC+ shifts revealed increased electron density and the image of spatial distribution of n_e. This method consists of an analysis of PL limitations in materials

with spatially nonuniform compositions. It provided key information to solve the complicated relation between radiative, non-radiative, spatial fluctuation of electron density, heat energy transport, and electron or hole transport properties. The result of the present analysis of images in the local region of high nonradiative recombination rate the local temperature increase was observed. In this region, the PL emission efficiency defined as the PL intensity per electron was found to be lower than that in the surrounding region.

References

[1] T. Nakayama, K. Ito, B. Ma, D. Iida, M. A. Najmi, K. Ohkawa, Y. Ishitani, Mater. Sci. Semicond. Process. 2022, 150, 106905.

[2] S. Okamoto, N. Saito, K. Ito, B. Ma, K. Morita, D. Iida, K. Ohkawa, Y. Ishitani, Appl. Phys. Lett. 2020, 116, 142107.

[3] M. Kuball, J. W. Pomeroy, IEEE Trans. Dev. Mater. Reliab. 2016, 16,667.

[4] Y. Ishitani, M. Fujiwara, T. Shinada, X. Wang, S. B. Che, A. Yoshikawa, Phys. Status Solidi C 2007, 4, 2428.

[5] K. Wang, R. R. Reeber, Appl. Phys. Lett. 2001, 79, 1602.

[6] X. Wang, S.-B. Che, Y. Ishitani, A. Yoshikawa, Appl. Phys. Lett. 2006, 89, 171907.

[7] V. Y. Davydov, Y. E. Kitaev, I. N. Goncharuk, A. N. Smirnov, J. Graul, O. Semchinova, D. Uffmann, M. B. Smirov, A. P. Mirgorodsky, R. A. Evarestov, Phys. Rev. 1998, 58, 12899.

[8] Y. Oshima, T. Suzuki, T. Eri, Y. Kawaguchi, K. Watanabe, M. Shibata, T. Mishima, J. Appl. Phys. 2005, 98, 103509.

[9] O.Kolomys,B.Tsykaniuk,V.Strelchuk,A.Naumov,V.Kladko,Y.I.Mazur, M. E. Ware, S. Li, A. Kuchuk, Y. Maidaniuk, M. Benamara, A. Berlyaev, G. J. Salamo, J. Appl. Phys. 2017, 122, 155302.

[10] V. Y. Davydov, N. S. Averkiev, I. N. Goncharuk, D. K. Nelson, I. P. Nikitina, A. S. Polkovnikov, A. N. Smirnov, M. A. Jacobson, O. K. Semchinova, J. Appl. Phys. 1997, 82, 5097.

[11] G. Callsen, J. S. Reparaz, M. R. Wagner, R. Kirste, C. Nenstiel, A. Hoffmann, M. R. Phillips, Appl. Phys. Lett. 2011, 98, 61906.

[12] X. D. Pu, J. Chen, W. Z. Shen, H. Ogawa, Q. X. Guo, J. Appl. Phys. 2005, 98, 033527.

[13] V. Darakchieva, P. P. Paskov, E. Valcheva, T. Paskova, B. Monemar, M. Schubert, H. Lu, W. J. Schaff, Appl. Phys. Lett. 2004, 84, 3636.

[14] B. Song, J. K. Jian, G. Wang, H. Q. Bao, X. L. Chen, J. Appl. Phys. 2007, 101, 124302.

[15] Y. Ishitani, Jpn. J. Appl. Phys. 2014, 53, 100204

[16] A. Kasic, M. Schubert, S. Einfeldt, D. Hommel, T. E. Tiwald, Phys. Rev. B. 2000, 62, 7365.

[17] C. E. Dreyer, A. Jano, tti, C. G. Van de Walle, Appl. Phys. Lett. 2013, 102, 142105.

[18] M. A. Moram, Z. H. Barber, C. J. Humphreys, J. Appl. Phys. 2007, 102, 023505.

CHAPTER 4
Local Augmentation of Phonon Transport at $Ga_{1-x}In_xN$/GaN Heterointerfaces

Abstract

The pump and probe technique in Raman spectroscopy of the E_2(High) (E_2^H) mode is a method using two laser pulses to study the heat energy transport in the material. The phonon transport process across the heterointerfaces is the factor dominating the thermal conductivity in multilayer structures of semiconductors. In this chapter, the transport process at the interface of GaInN/GaN is investigated. Two samples of $Ga_{0.91}In_{0.09}N$ /GaN (sample A) and another one with a graded variation in x from 0.17 to 0 along the depth direction in $Ga_{1-x}In_xN$ (sample B) are utilized. Lateral phonon transport can be examined by scanning the 532 nm probing laser from the irradiation position of the 325 nm heating laser. The transport across the interface is analyzed by the irradiation of these two lasers at the same position. The microscopic images of the decrease in the mode energy or the increase in the temperature of the GaN layer reveal the local phonon transport across the heterointerfaces between the GaN and GaInN. It is found that the agreement E_2^H mode energy between the two layers forming the heterointerface enhances the phonon transport.

4.1. Introduction

Electronic devices consist of multiple layers with thicknesses from nanometers to micrometers. The thickness of 100 nm of the GaN films has a thermal conductivity less than 10% that of 10 μm thick GaN. It indicates that the reduction of the thermal conductivity affects. This knowledges highlights the significant impact of the study on phonon transport at heterointerfaces. Additionally, the experimental transport processes remain unclear. The information on local thermal conductance properties across interfaces of epitaxial layers is significantly limited. The local blocking of phonon transport across the defective interfaces has already been reported using microscopic Raman imaging [9,10]. However, more experimental information is necessary on the energy transportation efficiency at semiconductor heterointerfaces.$Ga_{1-x}In_xN$ alloys covering the bandgap energy range of 0.63 [1] ~ 3.4 eV at room temperature. This bandgap range is used for applications for blue to green light-emitting diodes. The spatial nonuniformity of alloy composition leads to significant nonuniformity of strain variations because of the lattice mismatch of 11% between InN and GaN [3-5]. Thus, it enhances the nonuniformity of electronic and phononic energy structures [2,6,7,8]. Now, this alloy system is applied to red light-emitting diodes because thermal issues in micro LED structures are significant in investigating.

4.2. Experiment

In this study, the two samples with different InN mole fractions of the $Ga_{1-x}In_xN$ film are utilized. Sample A, $Ga_{1-x}In_xN$ film with a nonuniform system of InN mole fraction of 0.09 and sample B, $Ga_{1-x}In_xN$ film with a graded variation of InN mole fraction of 0.17 to 0 along the depth direction. These two GaInN layers have the thickness of 100 nm and 110 nm, respectively. The $Ga_{1-x}In_xN$ films of these sample were grown on n^+-GaN (3.5 μm) templates on the Sapphire substrates [2,6] by using the metal-organic vapor phase epitaxy (MOVPE) system. The electron density value of the n^+-GaN was 3×10^{18} cm^{-3}. It has been reported that the residual electron density of the GaInN layer of sample A was found to be less than 7×10^{16} cm^{-3} from the analysis of LOPC modes of an infrared (IR) spectrum analysis [11]. In that report, it is used the static and high-frequency limits of the dielectric constant of $9.8\varepsilon_0$ and $5.2\varepsilon_0$, respectivity, where ε_0 is the dielectric constant in the vacuum. Additionally, the effective electron mass is 0.21 m_0, where m_0 electron rest mass. Figure 4.1 expresses the reciprocal space

maps for the $(10\bar{1}5)$ diffraction of X-ray (Cu $K\alpha_1$ line:1.54 Å) and atomic force microscope (AFM) imgae of a GaN template. The full width at half maximum (FWHM) values of the (0002) rocking curve was obtaind as 320 arcsec for the $Ga_{0.95}In_{0.05}N$ layer and 340 arcsec for the GaN layer. The rocking curve width for the $(10\bar{1}2)$ diffraction for the GaN layer was 468 arcsec. Here, the formation of threading dislocations (TDs) at grain boundaries is assumed [12,13], which includes mixed-type one for the GaN layer. The densities of $Ga_{0.95}In_{0.05}N$ and GaN was found to be 2×10^8 cm^{-2} and 2×10^9 cm^{-2}, respectively. The density of the nodal points of atomic steps in the AFM image agrees with the density of 2×10^8 cm^{-2}. Sample A was 6% lattice relaxation. Sample B was pseudo-morphologically grown on the GaN template. It has been reported that the generation of misfit dislocations was suppressed by using a graded x variation to 0.16, which was observed in tunneling electron microscope images [2]. In addition, no clear dark line due to misfit dislocation was observed in the present PL intensity images. Figure 4.2 shows an example photoluminescence (PL) intensity (I_{PL}) and PL peak energy (E_{PLP}) image of the 1μm square gold (Au) film patterns with a distance of 10 um deposited on sample B. In each image of I_{PL}, Au film patterns are observed as four dark regions at the GaInN layer in the image of peak energy (E_{PLP}). The Au films possibly induce tensile strain in the GaInN and that strain affects little outside the pattern. However, this effect is not recognized in the GaN layer. The observation position can be identified at every measurement by using this Au pattern. The thickness of this Au film was 20 nm, and some of the PL is transmitted through this Au film.

Raman measurement system is exploited with the double laser systems 532 nm (signal probing) and 325 nm (heating and signal probing) to investigate the E_{E2H} of the GaInN and GaN films [9,10]. Backscattering was observed when the laser incident perpendicularly on the sample surface. No polarization selection was conducted. The heating is induced by the energy relaxation of photo-excited electrons and holes. The NR processes is a heating source[14]. The microscopic system was in a chamber and the temperature was kept as a constant temperature by controlling a gas flow into a chamber. Thus, the sample temperature was kept at 296 K. In the observation system, the monochromator with a focal length of 81cm, a grating of 2400 or 3600 grooves per mm, and a CCD camera were utilized. An objective lens with an NA of 0.47 was utilized. The FWHM of the Rayleigh scattering signal peak was measured to be 0.02 cm^{-1}.

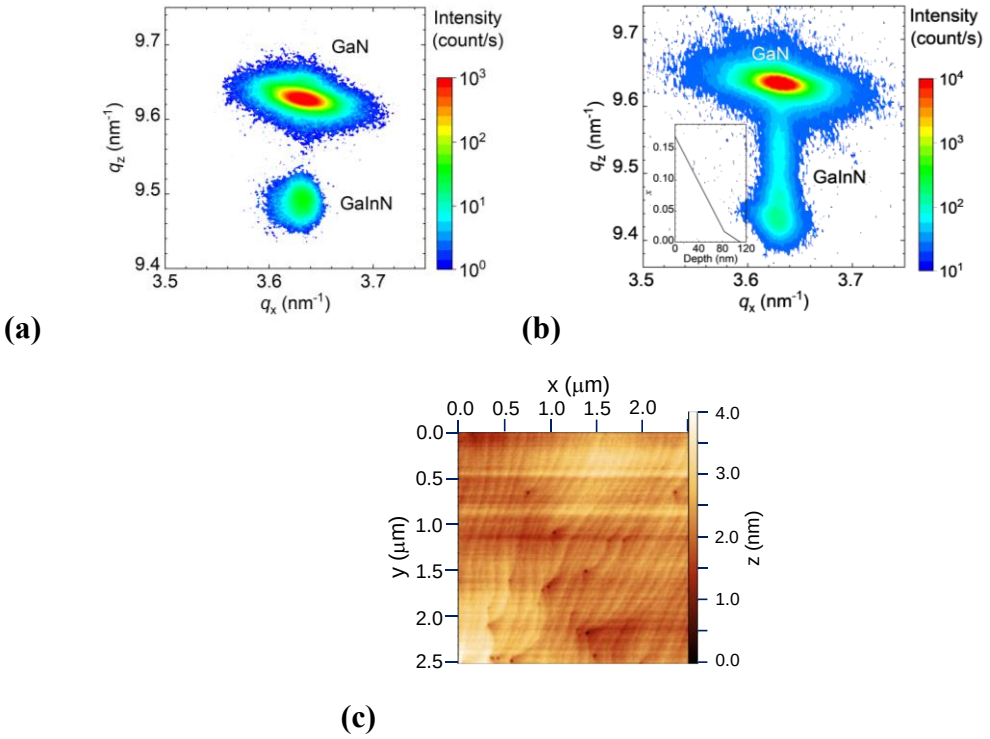

Figure 4.1. (a) Fundamental crystal-structural properties: reciprocal space mapping images of $(10\bar{1}5)$ X-ray diffraction for (a) sample A and (b) sample B, and (c) AFM image of the GaN template [9]. The profile of *x* of sample B is plotted in the inset of (b).

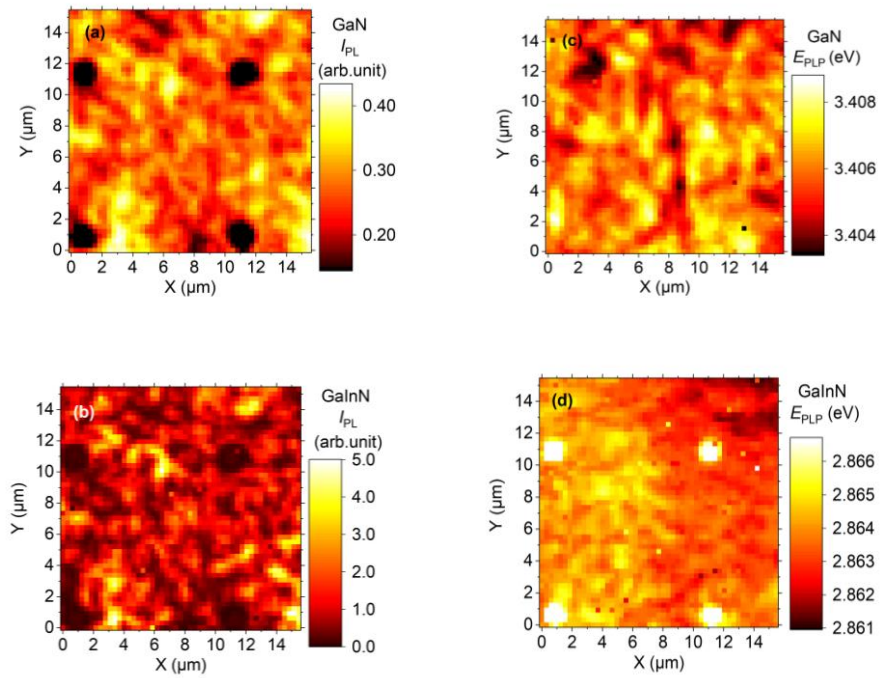

Figure 4.2. PL mapping images of sample B at 0.8 mW with 325 nm laser power (a) I_{PL} of the GaN layer (b) I_{PL} of the GaInN layer (c) E_{PLP} of the GaN layer (d) E_{PLP} of the GaInN layer.

The instrumental spectral resolution of the FWHM of a peak was 0.4 cm^{-1}. A more precise energy resolution was obtained by fitting the spectrum. The energy resolution of the spectrum peak relies on the signal-to-noise (SNR) ratio of the spectrum intensity. During the measurements of the GaN underlayer, high resolutions ranging from 0.015 to 0.03 cm^{-1} were achieved depending on the position through spectrum fitting. The lower resolutions between 0.1 and 0.2 cm^{-1} were observed for the GaInN layers. When two beams of different wavelengths were simultaneously incident on the sample, the 532 nm light was focused to a diameter of approximately 0.65 μm, whereas the 325 nm light was diffused to a diameter of approximately 7 μm. The reduction in ΔE_{E2H} energy was investigated. When the 532 nm laser is used for irradiation, the entire region of a 3.5 μm thickness of the GaN layer is expected to be observed. For sample A, the relaxation energy of an excited electron-hole pair to the band bottom is expected to be 20.8 (±0.8) percent of the excitation photon energy. The relaxation energy of sample B is calculated to be 18.4% when accounting for the graded variation in x and an absorption coefficient of 1/70 nm^{-1} [38]. The variation in x gained from the growth recipe is expressed in the insert of Figure 4.1 (b). The Raman images in the x-y plane were analyzed by scanning the sample position or laser irradiation spot. The Raman peak energy of E_{E2H} for the GaInN layer was measured by varying the power of the 325 nm laser-focused on the sample surface. The density of free carriers generated by the 325 nm beam was estimated to be less than $1x10^{18}cm^{-3}$ when considering the carrier lifetime. The consideration of carrier lifetime is approximately 100 ps or less, and the extension of the 2 μm volume occupied by the excited carriers is due to the carrier diffusion and repeated emission and reabsorption processes [39]. The occupied volume was estimated by observing the reduction in I_{PL} as the distance between the observation and excitation positions increased. Additionally, the excited electron density is estimated to be 10^{16} cm^{-3} for an excitation laser power of 1 mW when the sample is irradiated simultaneously with the two laser systems. The consideration of the thermal conduction by the free carriers is negligible in this study. Raman imaging of PL peak energy E_{PLP} and I_{PL} was conducted at 296 K by using the 325 nm laser in the same optical system. Figure 4.3 illustrates the schematic diagram of the laser irradiation and measurement conditions used in the Raman scattering spectroscopy.

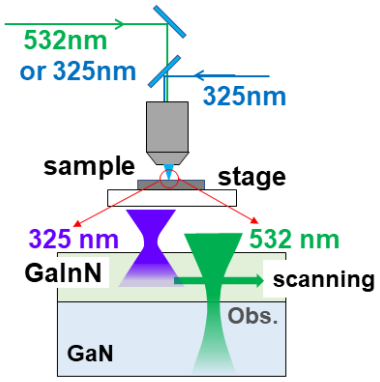

Figure 4.3. Schematic diagram of the laser irradiation and measurement in Raman spectroscopy.

4.3. Characteristics of Raman Spectra of E_{E2H} Modes in $Ga_{1-x}In_xN$ / GaN

Figure 4.4 shows example spectra probed using the 532 nm and 325 nm lasers in samples A and B. The blue-filled cycle curve of the spectrum is the E_2^H mode of the GaN underlayer using the 532 nm laser. The other two spectra correspond to the E_2^H mode of the GaInN film layer using 325 nm laser. According to the result, the phonon energy of the E_2^H mode of the GaInN layer shows a greater strain effect compared to the GaN layer. In sample A, the spectrum is broadened according to this factor,

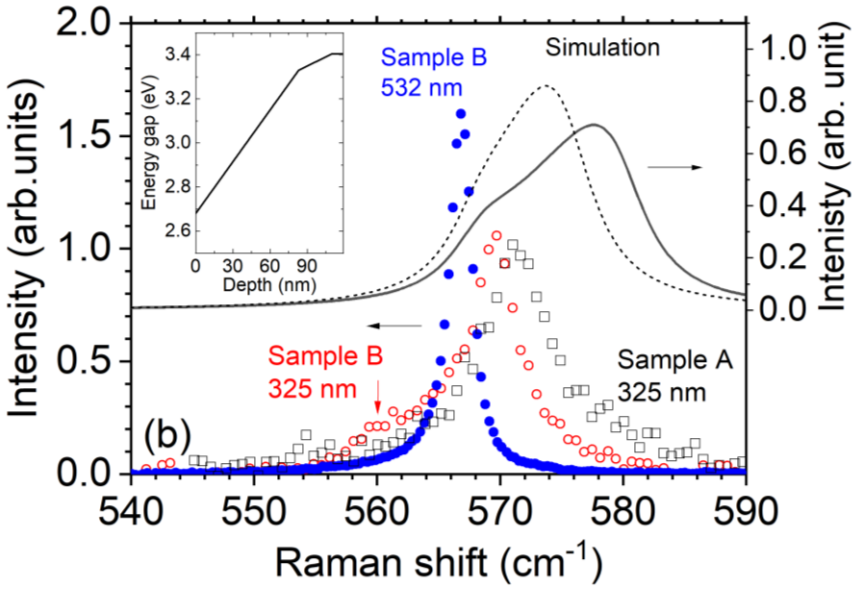

Figure 4.4. Example of Raman spectrum of sample A and B at 532 nm laser 325 nm laser excitation.

including that is the nonuniform strain and alloy composition and temperature. In sample B, the spectrum is a significant shoulder structure in the lower energy side of the peak. According to the calculation of the GaInN spectra of sample B by the solid and dashed curves, the calculated spectrum shape agrees with the experimental results. In this calibration, The calculation process takes into account the laser intensity attenuation with depth from the surface according to the absorption coefficient of 1.4×10^5 cm^{-1} [15] and the depth profile of E_2^H mode as a function of x and the biaxial strain ε . The estimated variation of energy gap (E_g) is plotted in insert of Figure 4.4. The dependence of E_{E2H} on ε is obtained from the Equation 4.1 [23].

$$E_{E2H} = E^0_{E2H}(x) - \left(2a - 2b\frac{v}{1-v}\right).\varepsilon \quad (4.1)$$

where, a,b, v, and $E_{E2H}{}^0(x)$ are compressive and shear deformation potentials, Poission ratio, and E_{E2H} of unstrained $Ga_{1-x}In_xN$, respectively. In addition, the values of the $Ga_{1-x}In_xN$ were obtained by the linear interpolation of the respective values of GaN and Indium Nitride (InN). The two dimensional stress condition is assumed on the basis of the pseudo morphological growth. Thus, the in-plane lattice constant of the GaInN layer equals that of GaN. Moreover, the main peaks and the shoulder structure are attributed to the Raman signal from the regions near the surface with high InN and lower InN mole fractions, respectively. However, there is a possible reason for the discrepancy in the peak energy position because of these factors. Peak position in the simulation depends on the specific set of deformation potential. In Figure 4.4, the solid line [16] was obtained by using a previous report [17] based on the consistency of the mode energy, strain, mole fraction, and electron density when varying the temperature of a sample with x = 0.05. The dashed line is used a different set of deformation potentials [18]. However, the peak energy reduces when the temperature increases, according to experimental results. The shift of 1 cm^{-1} was estimated by increasing the 325 nm laser power by from 0.7 mW to 9 mW, with a temperature increase ΔT of 94 K [17]. However, a local temperature increase in a few tens of nanometers on the surface side and a nonthermal distribution of phonon energy due to the acoustic phonon generation from the LO phonon induced by the electron energy relaxation are possible.

These issues are beyond the resolution of the detection system and analytical formula described in Equation 4.2. The reduction in ΔE_{E2H} as a function of ΔT was determined using the following equation. It is an approximated expression comprising

the two terms of the energy shift of bulk material $\frac{\partial E2H}{\partial T}\Delta T$ and the effect of thermal strain.

$$-\Delta E_{E2H}(\Delta T) = \frac{\partial E2H}{\partial T}\Delta T - \left(2a - 2b\frac{v}{1-v}\right).l_{th}//.\Delta T \qquad 4.2$$

where, l_{th} is the linear thermal expansion coefficient in tha $a-b$ plane. The value of the Table 4.1 parameter are utilized. The temperature dependence l_{th} of GaN was obtained by linear interpolation between the two values are utilized as shown in Table 4.1. The ΔE_{E2H} of the GaInN layer in Sample B was not obtained due to the significantly high I_{PL} with increased 325 nm laser power. Therefore, a temperature (T) of 296 K was used under conditions without 325 nm laser irradiation. Integrating Equation 4.2 from 296 K to a T yielded a quadratic equation of T. The solution to this equation provides a ΔT of 24 K for a ΔE_{E2H} = 0.1 cm^{-1} in the GaN layer, using the data from Table 4.1 with the deformation potential of E_{E2H} mode a = -911 cm^{-1} and b = -852 cm^{-1}.

4.4. Characteristics of Lateral Phonon Transport in $Ga_{1-x}In_xN$/GaN Heterointerfaces

Figure 4.5 shows the ΔE_{E2H} value measured using the 532 nm laser, while the 325 nm laser irradiates that indicating the corresponding ΔT in the GaN layer. This shift is plotted as a function of the distance between the 325 nm and 532 nm laser irradiation spots, while the position of the 325 nm laser irradiation is fixed constant. For a GaN

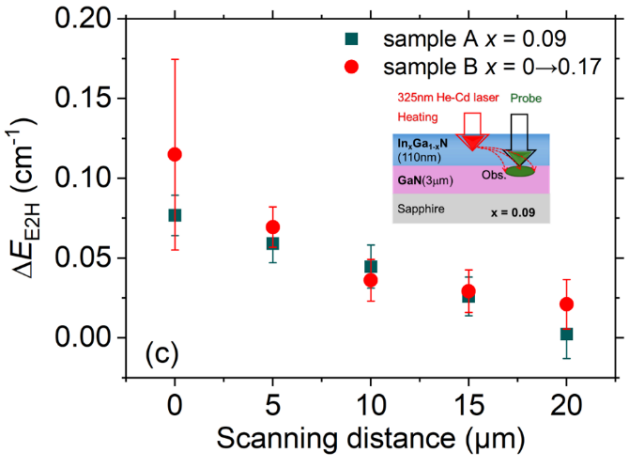

Figure 4.5. The ΔE_{E2H} as a function of the difference scanning distance with two lasers spot of heating and probing.

layer sample without any GaInN layer, the ΔE_{E2H} was determined to be less than 0.05 cm^{-1}. In most regions of sample A, this shift was observed to be less than 5% ΔE_{E2H} of GaN when the same laser power was applied. This low value of ΔE_{E2H} is consistent with the higher thermal conductivity of GaN. It indicates that the observed ΔE_{E2H} mainly reflects the lateral phonon transport within the $Ga_{1-x}In_xN$ layer rather than in the GaN layer from the 325 nm laser irradiation position.

4.5. Characteristics of Phonon Transport Across the Heterointerfaces in $Ga_{1-x}In_xN$/GaN

A histogram of the ΔE_{E2H} for the GaN template indicating the results with both lasers is incident in the same position as shown in Figure 4.6. This figure shows that sample B exhibits regions with higher ΔT compared to sample A, even though both samples have a nearly identical average x value of 0.085 (sample B) compared to 0.09 for sample A. There are three possible factors expressed. Firstly, the higher phonon transport across the interface in various regions of sample B. Secondly, increased phonon transport both laterally and across the interface in sample B due to the factor of a higher heat energy generation rate. Thirdly, the heat energy generation position is different within the GaInN films. The same identical gradient of E_{E2H} in Figure 4.6 between the two samples indicates the same ΔT, indicating that the lateral phonon transport flux is mostly the same between the two samples. Based on these factors, the transport across the interface is believed to be enhanced in sample B compared to sample A. Thus, the first factor is supporting while the second and third factors is

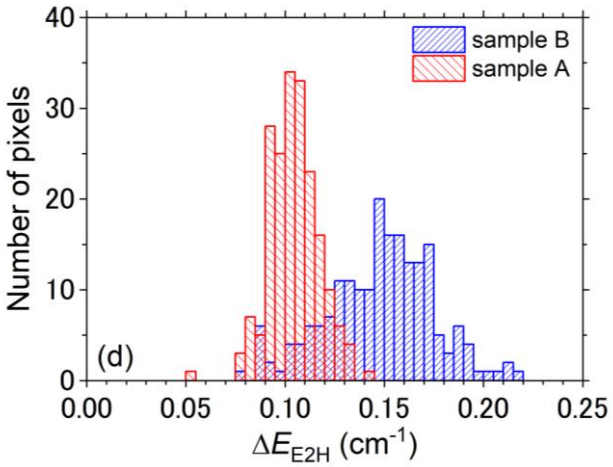

Figure 4.6. Histogram of the distribution of ΔE_{E2H} at sample A and B.

excluding. Thus, the lower energy bandgap on the surface side of sample B suggests a higher heat energy generation rate on the surface side.

4.6. Phonon Transport Analysis Heterointerfaces in $Ga_{1-x}In_xN$ / GaN with graded increase in *x* toward the surface (sample B)

The Raman mapping imaging of E_{E2H} values of the GaN with 532 nm laser and GaInN layers with 325 nm (5 mW) laser in the same regions of sample B as shown in

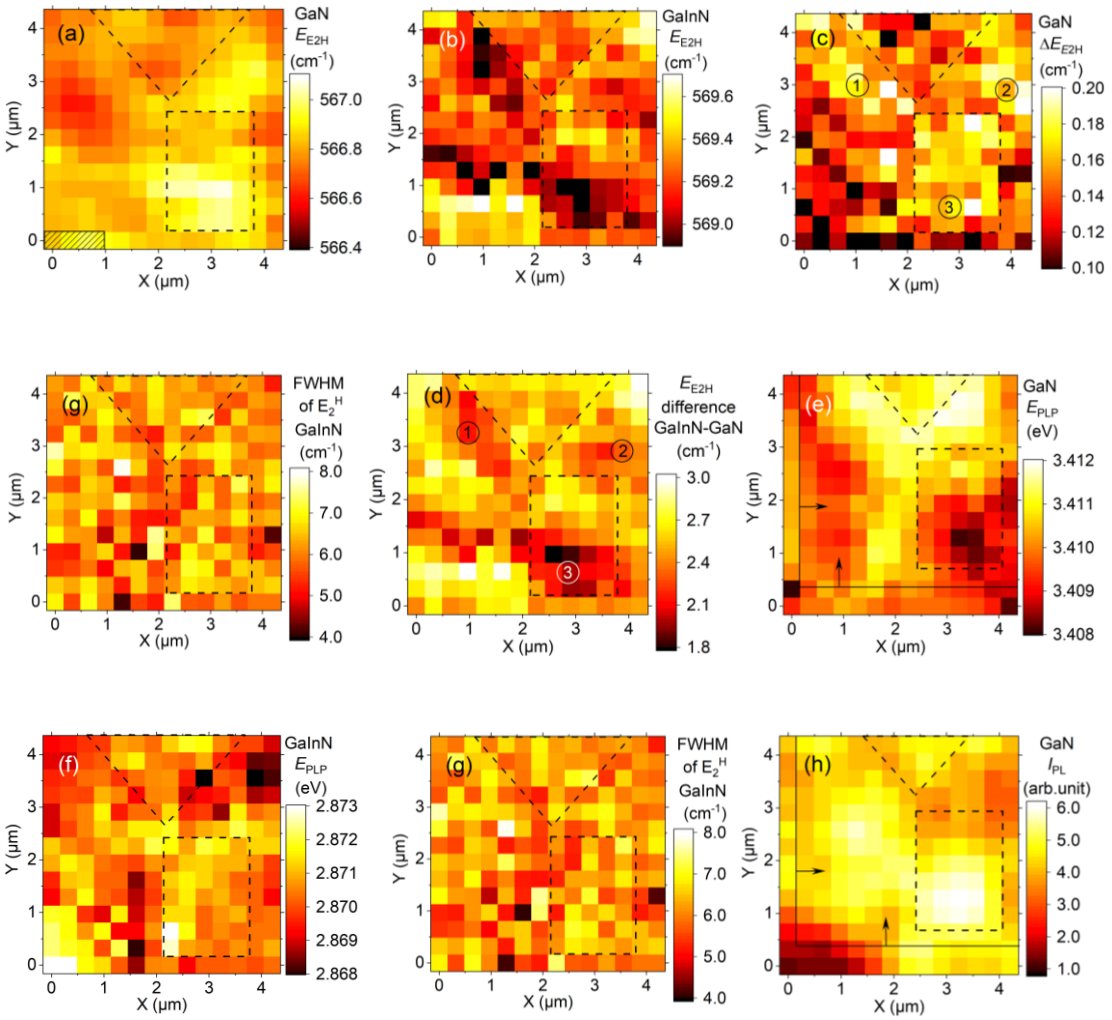

Figure 4.7. Mapping images of Raman and PL properties of Sample B (a) E_{E2H} of GaN (b) E_{E2H} of GaInN (c) ΔE_{E2H} of the GaN layer by the irradiation of the 325 nm laser (d) difference in E_{E2H} between the GaInN and GaN layers, (e) E_{PLP} of GaInN (Γ) FWHM of E_{E2H} of the GaInN layer, and (h) I_{PL} of GaN. Note that the hatched region in (a) is covered by an Au plate. The 325 nm laser powers are 5 mW and 16 mW for the Raman measurements of the GaInN and GaN layers, respectively, and 0.8 mW for the PL measurement.

Figure 4.7 (a) and (b). The ΔE_{E2H} of the GaN layer was measured by irradiating the 325 nm laser at a power of 16 mW in the same region as shown in Figure 4.7 (c). The inside of the squares region indicated by the arrows is the commonly observed region by the measurements using 532 nm and 325 nm lasers. The ΔE_{E2H} or ΔT values of the GaN layer in the vicinity of positions ①, ②, and ③ are higher than those in the surrounding regions. Figure 4.7 (d) reveals that the difference in E_{E2H} between the two layers is low in these regions. This result shows that phonon transport is increased at an interface consisting of a compressively strained GaN layer and a GaInN layer with a low InN mole fraction. The photoluminescence energy (E_{PLP}) values of the GaN and GaInN layers are shown in Figures 4.7 (e) and (f), respectively. The high E_{PLP} values of the GaN and GaInN layers in the vicinity of positions ① and ②indicate high energy gap of GaN and GaInN in the local regions. This observation is consistent with the compressive strain in GaN and the low In content (x) in $Ga_{1-x}In_xN$, which suggests a lower compressive strain in the GaInN layer. The factor of higher energy generation rate due to the laser excitation in these regions is excluded because of the higher energy gap values. Figure 4.7 (g) shows the image of the FWHM value of the E_{E2H} peak, showing no structural features as exhibited in Fig. 4.7 (c). This result indicates the factor dominating the phonon transport rate has no relation with crystal quality. Figure 4.8 shows I_{PL} and errors in E_{E2H} of the GaN and GaInN layer of sample B. I_{PL} is thought to be affected by the gradient of the potential or E_g in the present confocal measurement system. Thus, I_{PL} is weak in the region where the generated carriers escape to other regions. The I_{PL} is weak in the vicinity of the positions of ① and ②. In these regions, the E_{PLP} is found to be high in Figure 4.7 (f). Carriers are estimated to be transported to the lower potential regions. In region ③, high E_{PLP} and I_{PL} show lower NR probability in the GaInN layer than other regions, which denies the high energy generation by the NR process. The images of errors in E_{E2H} of GaN and GaInN have high values in some regions, while these images exhibit no structures correlated with regions ①, ②, or ③. The uncertainties of E_{E2H}s of GaInN and GaN are equal to or less than 0.1 cm^{-1} and 0.015 cm^{-1}, respectively.

The high E_{E2H} and low E_{PLP} of GaN at position ③ cannot be clarified by the model of two-dimensional stress. The high photoluminescence intensity I_{PL} in this region of GaN shown in Figure 4.7 (h) indicates a low density of NRC center which means a low phonon generation rate and lesser blocking effect of phonon transport [29].

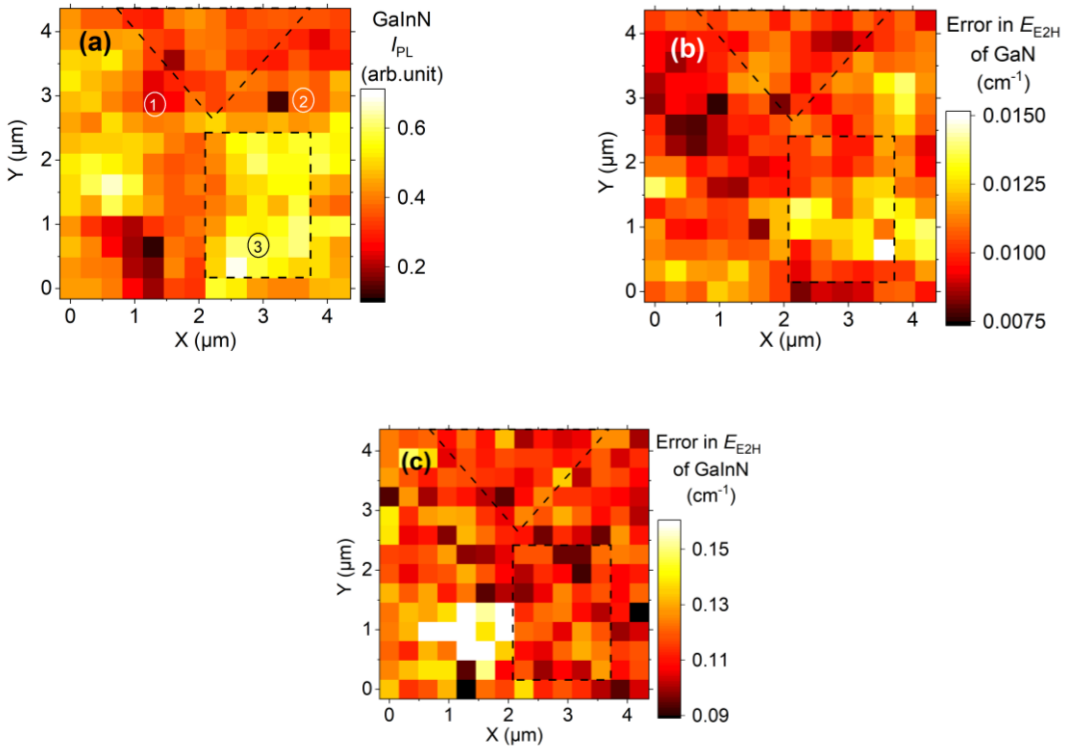

Figure 4.8. Raman and PL of Sample B (a) I_{PL} of the GaInN layer (b) error in E_{E2H} of the GaN layer and (c) error in E_{E2H} of the GaInN layer in the images in sample A.

4.7. Phonon Transport Analysis with Raman Imaging in $Ga_{1-x}In_xN$ /GaN Heterointerfaces (x=0.09)

Figure 4.9 shows the data of sample A. E_{PLP} of the GaInN layer shows high energy, indicating low InN mole fraction in the region of high ΔE_{E2H} of the GaN layer. The error in E_{E2H} of the GaInN layer shown in Figuure 4.9 (b) is high compared to GaN template layer and the GaInN layer of sample B, while this error is lower than the variation in E_{PLP} of the GaInN layer. The error of ΔE_{E2H} of the GaN layer in Figure 4.9 (c) shows the variation in ΔE_{E2H} , and Figure 4.9 (d) shows an image of I_{PL} in a large region. In this image, no dark line originating from misfit dislocations is identified.

In Figure 4.9, a high I_{PL} was observed in this region of the GaInN layer, indicating that the heat energy generated by carrier energy relaxation and NR processes in this region cannot be higher than that of other regions. When lattice relaxation takes place in the GaInN layer, E_{E2H} and E_g are expected to decrease in contrast with the values of the pseudo-morphological GaInN. In the vicinity of ① and ②, where the ΔE_{E2H} of the underlying GaN layer is higher than in other regions, the GaInN surface-

side layer exhibits lower E_{E2H} and higher E_g compared to the surrounding regions. Thus, the selective NR processes and phonon generation caused by lattice relaxation in these regions are ruled out from the candidate origins.

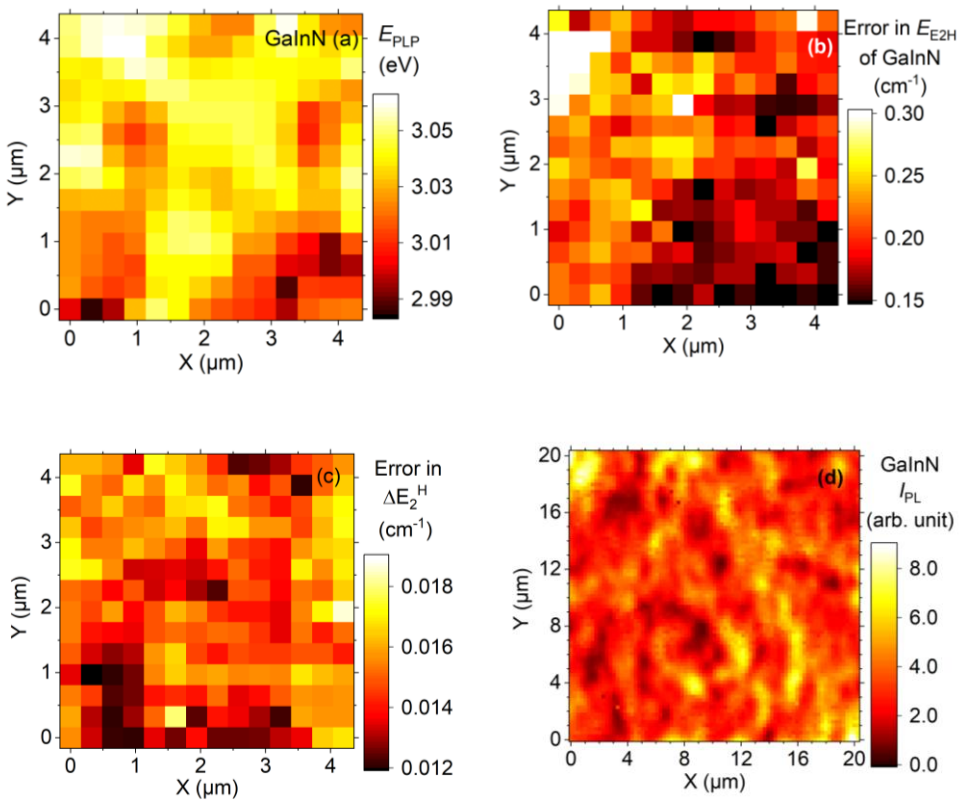

Figure 4.9. Raman and PL Sample A (a) E_{PLP} of the GaInN layer, (b) error in E_{E2H} the GaInN layer, (c) error in ΔE_{E2H} of the GaN layer, (d) PL peak intensity in a large area of the sample without Au patterning.

Since the present crystals are grown on a c-face surface, the heterointerface is considered to be negatively charged due to piezoelectric polarization, indicating that electron accumulation cannot take place at the heterointerface. Therefore, electron accumulation in the vicinity of the heterointerface cannot be the reason for the energy transport at the heterointerface. These results suggest that the lower discontinuity in phonon energy is the key factor dominating the phonon transport across the interface.

The observed difference in E_{E2H} between GaN and GaInN is approximately 3 cm^{-1}, which is reduced to 2 cm^{-1} in regions ① - ③. The impact of this difference on phonon transport is discussed. It is known that longitudinal optical (LO) phonons at the Γ point are generated as the initial step and then decompose into E_{E2H} and longitudinal acoustic (LA) phonons at the M critical point, or into E_1(TO) and LA phonons at the L-

point, with a time constant of approximately 3 ps or less [26]. These processes are followed by the decomposition of E_{E2H} and E_1(LO) phonons, occurring with a time constant of a few picoseconds [26], and those of the LA phonons with time constants of 5 – 300 ps [27]. As the conservation of energy and momentum are critical in these processes, the modulation of phonon energy by a few cm^{-1} due to structural variations, such as graded *x* potentially influence the decomposition processes in the vicinity of the interface.

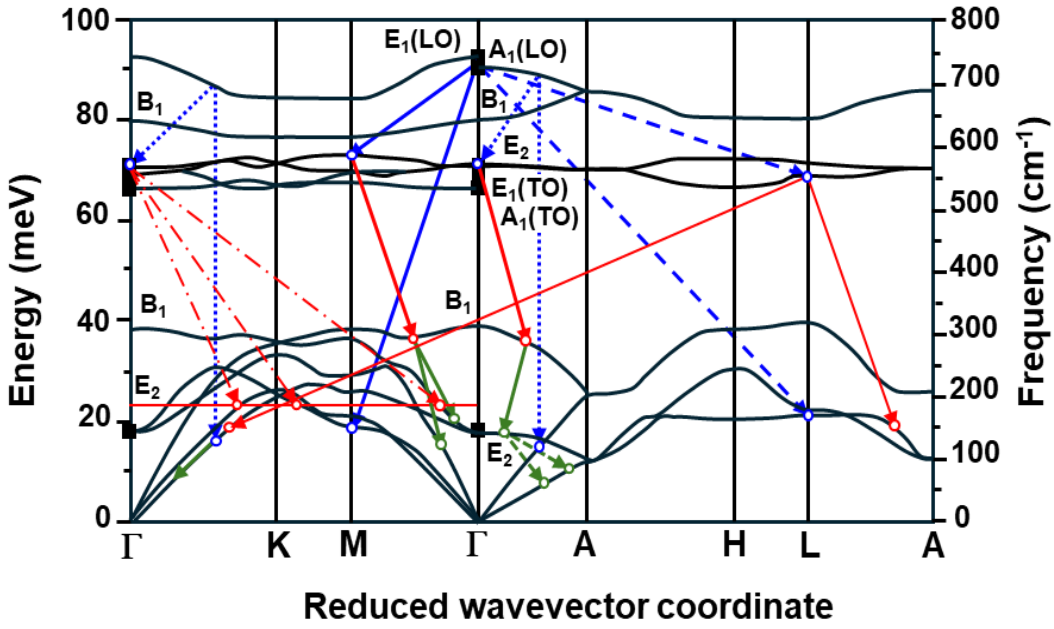

Figure 4.10. GaN of phonon dispersion curve.

Figure 4.10 shows the phonon energy dispersion curve [24-25]. This figure shows examples of estimated decay processes in GaN, which is E_{E2H} mode, which is an important mode for studying the phonon transport processes. The results show that the momentum relaxation of the LO phonon takes place in several picoseconds. Therefore, this process can be related to the interaction with generated electrons. According to the combination of the values of phonon energy modes of E_{E2L} and E_{E2H} is impossible from the viewpoint of energy conservation. As the excited electron density is estimated to be $2\times10^{16}cm^{-3}$ yields the lower energy branch of the LO phonon plasma coupling mode (LOPC-) at 25 cm^{-1}. Therefore, the decomposition of the E_{A1LO} phonon into the $E_{E2H}(\Gamma)$ and the LOPC- (Γ) phonon is not possible. It has been reported that 30% of the decomposition of E_{A1LO} phonon is attributed to the processes yielding E_{E1TO} (L) and TA (M) phonons [26]. The Umklapp processes in the decomposition of the E_{A1LO} phonons

to E_{E2H} and TA (M) phonons are also considered to be feasible. Thus, the E_{E2H} mode energy difference between the M and Γ points is feasibly within the energy uncertainty determined by the short lifetime of the E_{E2H} (M) phonon.

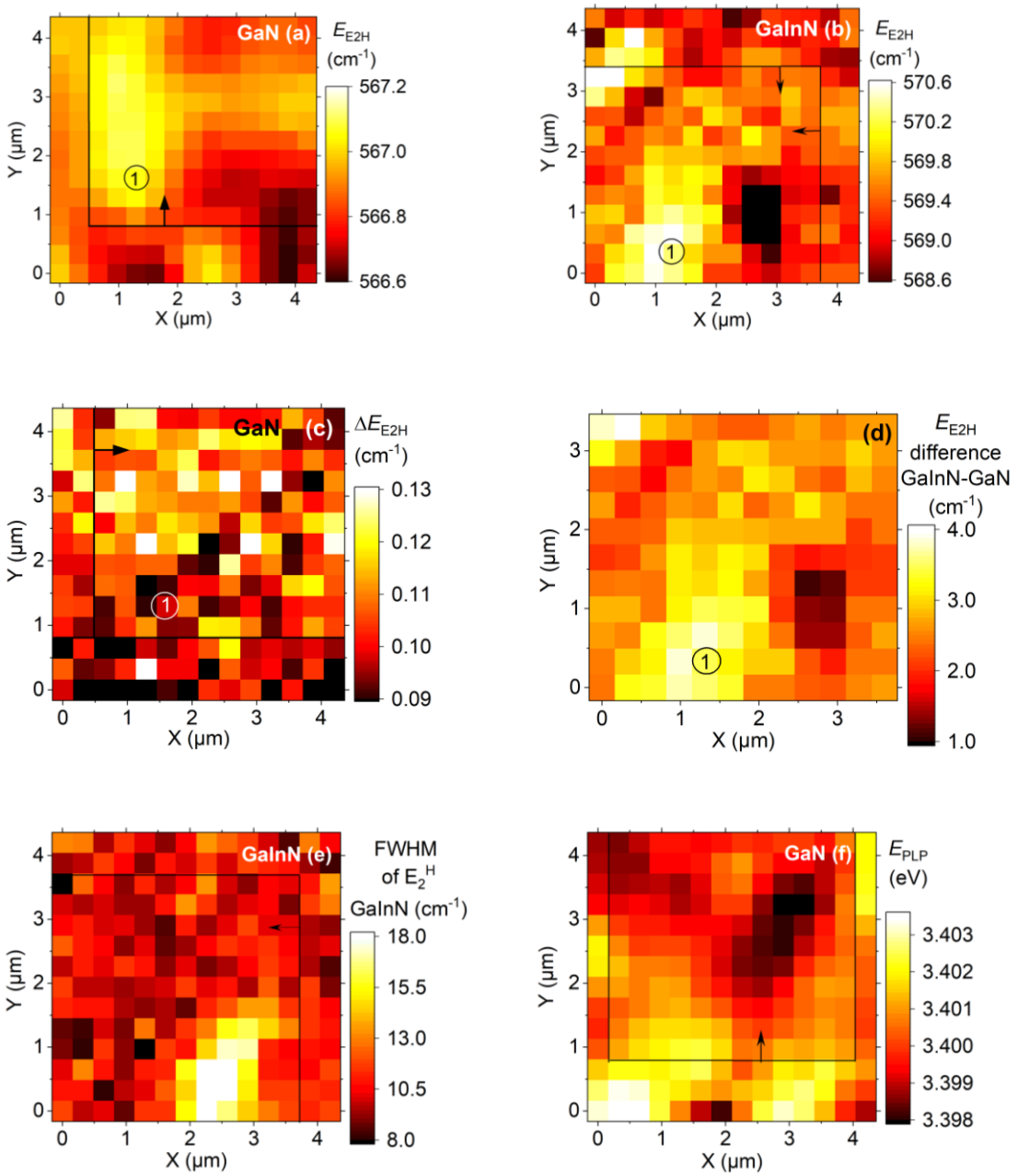

Figure 4.11. Mapping images of E_{E2H} of the (a) GaN layer and (b) the GaInN layer (c) ΔE_{E2H} of GaN by irradiating the 325nm laser (d) the difference in E_{E2H} between GaInN and GaN layers (e) FWHM of the E_{E2H} peak of GaInN (f) and PL peak energy of GaN. The laser excitation conditions are the same as those for Sample B.

Figure 4.11 shows the PL and Raman images of GaN and $Ga_{0.91}In_{0.09}N$ layers of sample A. The square region indicated with arrows is commonly observed using the

532 nm and 325 nm lasers. In Figure 4.11 (c), the ΔE_{E2H} of the GaN layer of sample A is lower than that of sample B when compared. The highest ΔT in this region is approximately 14 K. A low ΔE_{E2H} of the GaN layer is observed near position ①, which corresponds to the significant E_{E2H} difference between the GaN and GaInN layers in this region as shown in Figure 4.11 (a), (b), and (d). Figure 4.11 (e) shows the FWHM value of the GaInN layer where no correlation observed with Figure 4.11 (c) is identified. In this sample, the low difference in E_{E2H} between the layers comprising an interface is also considered to be the origin of the high rate of phonon transport across the heterointerface.

4.8. Conclusion

In conclusion, thermal energy transport at GaInN/GaN heterointerfaces was investigated using a Raman-scattering measurement system equipped with a heating laser and a signal-probing laser. Higher energy transport was observed at the $Ga_{1-x}In_xN$/GaN heterointerface with a graded variation in x (0 ~ 0.17) compared to the $Ga_{0.91}In_{0.09}N$/GaN heterointerface, despite the average InN fraction x of 0.085 for sample B being nearly identical to the x of 0.09 for sample A. The high thermal energy transport is attributed to the higher phonon transport from the lower phonon energy gap at the heterointerface for the E_2^H mode. This result is considered to the related to the LO phonon decomposition via E_2^H mode and the energy and momentum conservations at the heterointerface.

Table 4.1. Parameters for anisotropic strain and lattice vibration of GaN and InN

		a	b	v	l_{th}	$\partial\omega/\partial T$	ω_0
		(cm^{-1})	(cm^{-1})		($10^{-6}K^{-1}$)	($10^{-2}cm^{-1}K^{-1}$)	(cm^{-1})
GaN	E_2^H	-911[16]	-852[16]	0.183[19]	5.7(573K)[20]	-1.7[a]	567.6[21]
		-742[18]	-715[18]		4.2(296K)[20]		
InN	E_2^H	-610[22]	-857[22]	0.21[23]	4.0[26]	-4.1[a]	494.6[23]

References

[1] Y. Ishitani, Jpn. J. Appl. Phys. 53, 100204 (2014).

[2] K. Ohkawa, Y. Uetake, M. Velazquez-Rizo, and D. Iida, Nano Energy 59, 569 (2019).

[3] Y. Ishitani, M. Fujiwara, T. Shinada, X. Wang, S.-B. Che, and A. Yoshikawa, Phys. Sat. Sol. C 4, 2428 (2007).

[4] J. Wu, W. Walukiewicz, K.M. Yu, J.W. Ager III, S.X. Li, E.E. Haller, H. Lu, and W. J. Schaff, Sol. Stat. Commun. 127, 411 (2003) .

[5] Y. Zhao, H. Wanga, X. Gong, Q. Li, G. Wu, W. Li, X. Li, and G. Du, J. Lumin. 186, 243 (2017).

[6] K. Ohkawa, F. Ichinohe, T. Watanabe, K. Nakamura, and D. Iida, J. Cryst. Growth 512, 69 (2019).

[7] K. Kumakura, T. Makimoto, N. Kobayashi, T. Hashizume, T. Fukui, and H. Hasegawa, J. Cryst. Growth 298, 787 (2007).

[8] A. Vertikov, I. Ozden, and A. V. Nurmikko, J. Appl. Phys. 86, 4697 (1999).

[9] T. Nakayama, K. Ito, D. Iida, M. A. Najmi, K. Ohkawa, Y. Ishitani, Mater. Sci. Semicond. Process. 150, 106905 (2022).

[10] S. Okamoto, N. Saito, K. Ito, B. Ma, K. Morita, D. Iida, K. Ohkawa, Y. Ishitani, Appl. Phys. Lett. 116, 142107 (2020).

[11] M. Kuball, IEEE Trans. Device. Mater. Reliab. 16 , 667 (2016).

[12] S. R. Lee, A. M. West, A. A. Allerman, K. E. Waldrip, D. M. Follstaedt, P. P. Provencio, D. D. Koleske, C. R. Abernathy, Appl. Phys. Lett. 86, 241904 (2005).

[13] Y. Ishitani, K. Kato, H. Ogiwara, S.-B. Che, A. Yoshikawa, X. Q. Wang, J. Appl. Phys. 106, 113515 (2009).

[14] Y. Kawakami, K. Omae, A. Kaneta, K. Okawmoto, T. Izumi, S. Saijou, K. Inoue, Y. Narukawa, T. Mukai, Sg, Fujita, Phys. Stat. Sol. A 183, 41 (2001).

[15] J. F. Muth, J. H. Lee, I. K. Shmagin, and R. M. Kolbas, H. C. Casey, Jr., B. P. Keller, U. K. Mishra, and S. P. DenBaars, Appl. Phys. Lett. 71, 2572 – 2574 (1997).

[16] G.Callsen, J. S. Reparaz, M. R. Wagner, R. Kirste, C. Nenstiel, A. Hoffmann, M. R. Phillips, Appl. Phys. Lett. 98, 61906 (2011).

[17] T. E. K. Shwe, T. Asaji, R. Kimura, D. Iida, M. A. Najmi, K. Ohkawa, Y. Ishitani, Phys. Stat. Sol. B, 2024, 2400057 (2024).

[18] J.-M. Wagnera and F. Bechstedt, Appl. Phys. Lett. 77, 346 (2000).

[19] M. A. Moram, Z. H. Barber, and C. J. Humphreys, J. Appl. Phys. 102, 023505 (2007).

[20] Y. Oshima, T. Suzuki, T. Eri, Y. Kawaguchi, K. Watanabe, M. Shibata, and T. Mishima, J. Appl. Phys. 98, 103509 (2005).

[21] V. Y. Davydov, Y. E. Kitaev, I. N. Goncharuk, A. N. Smirnov, J. Graul, O. Semchinova, D. Uffmann, M. B. Smirov, A. P. Mirgorodsky, and R. A. Evarestov, Phys. Rev. 58, 12899 (1998).

[22] X. D. Pu, J. Chen, W. Z. Shen, H. Ogawa, and Q. X. Guo, J. Appl. Phys. 98, 033527 (2005).

[23] X. Wang, S.-B. Che, Y. Ishitani, and A. Yoshikawa, Appl. Phys. Lett. 89, 171907 (2006).

[24] H.Siegle, G.Kaczmarczyk, L.Filippidis, A.P. Litvinchuk, A Hoffmann, and C. Thomsen, Phys.Rev.B55,7000(1997).

[25] T.Beechem and S.Graham, J.Appl.Phys. 103, 093507 (2008).

[26] S. Barman, G. P. Srivastava, Phys. Rev. B 69, 235208 (2004).

[27] A. Cepellotti, J. Coulter, A. Johansson, N. S. Fedorova, B. Kozinsly, J. Phys. Mater 5, 035003 (2022)

CHAPTER 5

Fe-doped GaN with microscopic Raman spectroscopy analysis

Abstract

Fe-doped GaN is widely utilized as a semi-insulating material. The electron dynamics have been investigated, while some of the hole dynamics still remains unknown. We focus on the extraordinal nature of the temperature dependence of the longitudinal optical (LO) phonon – plasmon coupling (LOPC) in Fe-doped GaN. The difference in energy shifts of phonon modes between two heating conditions of thermal equilibrium case and laser heating in Raman spectroscopy is investigated. A 325-nm laser is used as the heating and probing laser, and a 532-nm laser is used to detect the Raman signals in GaN. An abnormal high mode energy shift to the lower energy side is observed for the laser-heating condition for the A_1(LO) mode but not for the E_2(high) mode. This phenomenon is more significant for samples with higher Fe densities. This phenomenon can be attributed to the energy shift of the higher energy branch of the LOPC modes to the lower energy side, which is possible for the coupling with hole-plasmon. This result suggests the domination of hole density in the photo-excited area by the fast capture of electrons by Fe atoms.

5.1. Introduction

GaN has properties of high bandgap energy of 3.4 eV at room temperature, high saturation velocity, and high critical electric field [1-4]. The development of growth technique in bulk GaN wafers is expected to enable the growth of epitaxial layers with low defect density, resulting in high carrier mobility [5-10] even with a thinner buffer layer as compared to the layers grown on Si, SiC, and sapphire [10.11]. However, high-density impurities can be introduced during growth [11-13], resulting in some undesired properties of crystals, e.g., n-type conduction despite non-doping conditions and leakage paths in the active region of the device [14-15]. A high-resistivity buffer layer is required to reduce the leakage [16,17], particularly in high-power devices. Iron (Fe) doping is commonly used to achieve high resistivity GaN layer [18-20].

The carrier dynamics in Fe-doped material have been reported in many papers. Electron capture, populating the Fe_{Ga}^{2+} state with free holes, after the band-band transition is followed by the radiative transition to $^6A_1$ state [21]. Ščajev *et al*. reported a high hole capturing cross section by analyzing the transient transmissivity after a pulse generation of electrons and holes using rate equations [22]. Although we can refer to several papers discussing electron and hole capture and transition processes related to deep levels [21 - 24], there are few reports on the density of electrons or holes remaining in the bands. The remaining carriers possibly yield the LO phonon – plasmon coupling modes and shift the A_1(LO) mode energy to the higher or lower region depending on the plasmon scattering rate.

It is known that E_2^H and A_1^{LO} of a wurtzite crystal are the allowed modes in Raman scattering when adopting the configuration of <-z, - - ,z> using a c-face sample. As the temperature derivative of A_1^{LO} energy is reported to have a higher value than that of the E_2(high) mode, the former mode is considered to be more sensitive to the temperature increase than the latter one. However, when a certain portion of carriers exist even in the Fe-doped GaN, the peak energy of the A_1(LO) mode can be varied by the carriers. When holes remains, it is difficult to estimate the density because of the low mobility and the resultant low rate coefficient of the capture by deep levels, even for a high cross section.

Many of the operational functions of electronic and photonic devices are suppressed by temperature increases. Therefore, the control and analysis of phonon

dynamics are indispensable. In this chapter, the mechanism of LO phonon between the two differences of bulk GaN and Fe-doped GaN was investigated.

5.2. Experiment

Three samples of Fe-GaN with high Fe density in the range of 5×10^{18} ~2×10^{19} cm^{-3}, sample N and sample S, and an undoped free-standing GaN wafer were investigated. The more yellowish color of sample N indicates the higher deep levels due to higher Fe density. It is known that Fe levels compensate the background electrons of GaN due to residual oxygen or Si, and give high resistivity [25]. We investigated the difference in energy shifts of phonon modes between two heating conditions of thermal equilibrium case and laser heating in Raman spectroscopy. A 325 nm laser was used as the heating and probing laser with different laser power excitation, and a 532 nm laser was used to detect the Raman signals under the sample uniform heating of wafers. When samples were heated by a Peltier device in a vacuum chamber, the temperature of the samples on the device was controlled between 296K to 400K, and the temperature was uniform in the sample. The temperature was monitored by a alumel-chromel thermocouple. A confocal optical system with an objective lens or mirror with NA in the 0.47 was utilized.

The excitation power density was controlled in a range of 3.1×10^{5} - 3.1×10^{6} Wcm^{-2}, indicating the generated electron density is estimated to be 1.1×10^{18} - 1.1×10^{19} cm^{-3}. Here, the carrier diffusion is neglected. This value is comparable to the Fe density in the GaN sample.

5.3. Temperature dependence with 532 nm laser excitation

Figure 5.1 shows an example of a Fe-GaN (Nanowin) sample of the Raman spectra of the E_2^H and A_1^{LO} modes of GaN as a function of thermal equilibrium temperature in the range of 300 K to 400 K. The 532 nm laser excitation was used. The ratio of $\Delta E_{A1LO}/\Delta E_{E2H}$ is approximately 2 and constant in the measurement temperature range and independent of the Fe-doping density. Thus, the variation in the degree of the anharmonicity of the lattice vibration can be neglected.

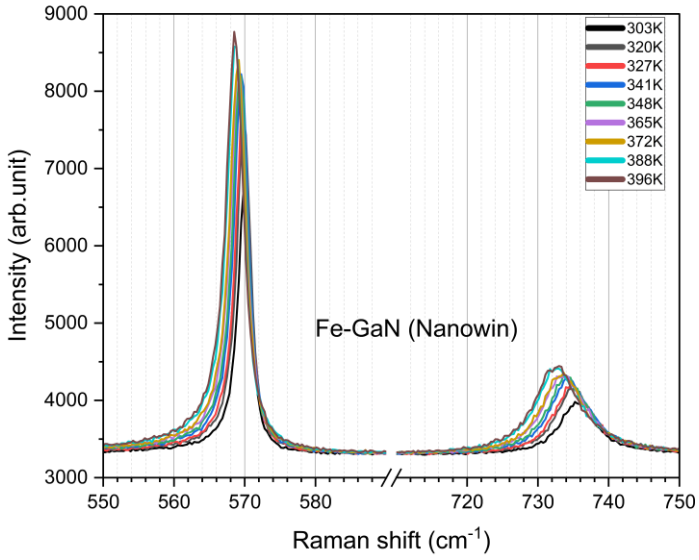

Figure 5.1. Example of the dependence of the spectrum of the 532 nm laser excitation on temperature for Fe-GaN (sample N).

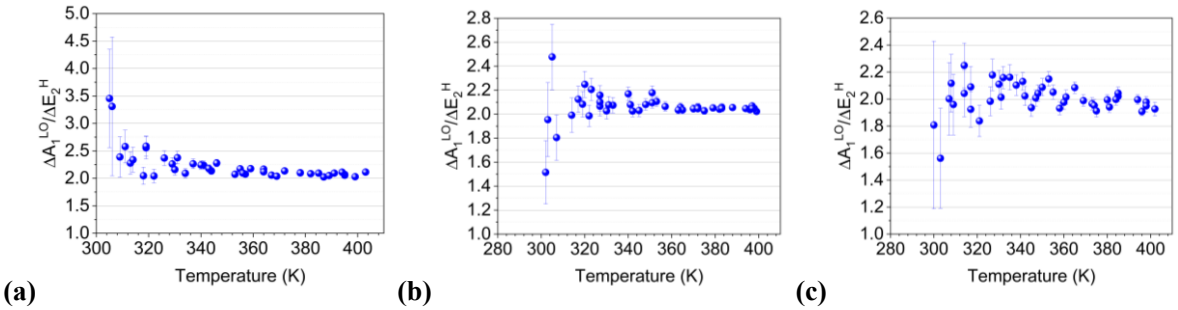

(a) (b) (c)

Figure 5.2. The ratio of the $\Delta E_{A1LO}/\Delta E_{E2H}$ obtained using the 532 nm laser as a function of temperature, (a) Fe-GaN (sample S), (b) Fe-GaN (sample N), and (c) bulk undoped GaN.

5.4. Power dependence with 325 nm laser excitation

Figure 5.3 shows an example of the dependence of Raman spectra by using the 325 nm laser excitation on the laser power. Figure 5.4 shows the histogram of the ratio of the shift of the A_1^{LO} mode energy ΔE_{A1LO}, and the shift of the E_2^H mode energy ΔE_{E2H}, $\Delta E_{A1LO}/\Delta E_{E2H}$, in a 3.0 -3.5 μm square region. ΔE_{A1LO} is over five times greater than ΔE_{E2H} in the case of laser heating, as shown in Figure 5.4. These values are unexpectedly high when considering the result of the previous section. It was reported that the electron mobility for the Si doping density over 10^{20} cm^{-1} is still higher than

100 cm^2/Vs [26], corresponding to the plasmon broadening of 450 cm^{-1}. In this case, the increase in the LOPC+ mode as the increase in electron density is expected, indicating higher energy than the LO mode energy; the ratio $\Delta E_{A1LO}/\Delta E_{E2H}$ lower than 2 is expected. Thus, the electron plasmon is excluded from the candidate origins. In contrast, when the broadening factor of plasmon is as high as 1000 cm^{-1}, overdamping condition, it is known that the higher energy branch of the LOPC mode energy decreases as the increase in the charge carrier density, which is typically identified for p-type materials [27]. Thus, the LO phonon−hole plasmon coupling is a probable candidate.

The abnormal high energy decrement in the A_1(LO) mode indicates electrons are firstly trapped, and the holes possibly remain. The high value of the hole capture cross section has been reported, while the diffusion length is quite low because of the high scattering rate of the plasmon.

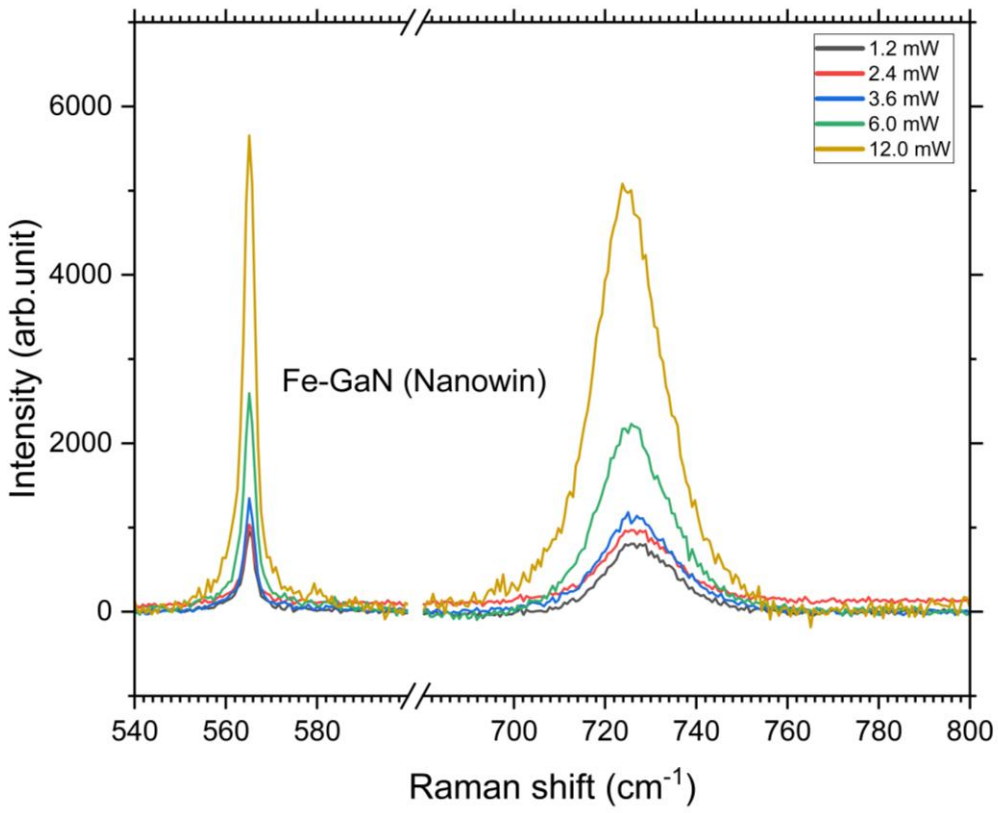

Figure 5.3. Example of the spectrum of the 325 nm laser excitation with different laser power of Fe-GaN (sample N).

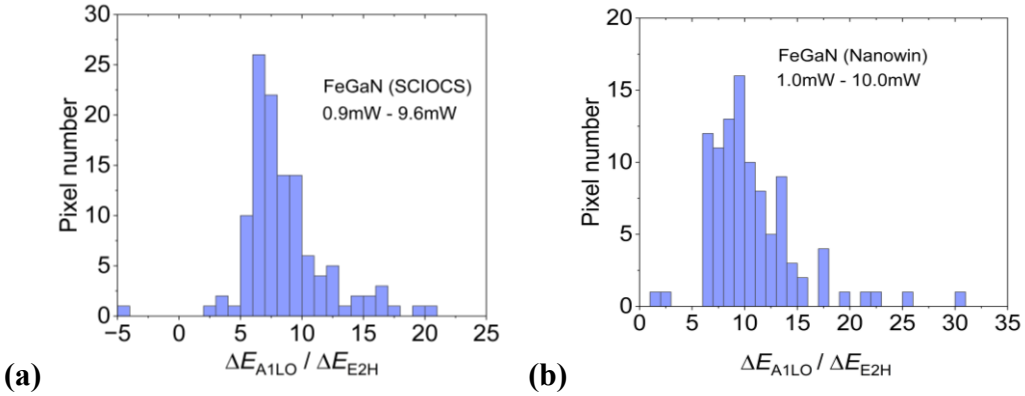

Figure 5.4. The ratio of the $\Delta E_{A1LO}/\Delta E_{E2H}$ with 325 nm laser excitation power of 1mW – 10mW (a) Fe-GaN (Sample S) and (b) Fe-GaN (Sample N).

5.5. Conclusion

In conclusion, Fe-doped GaN and bulk GaN were investigated using two heating conditions of thermal equilibrium and laser heating in Raman spectroscopy. The ratio of the value of energy decrement in A_1^{LO} mode is five times as high as the energy decrement in E_2^H mode or higher when heating by the 325 nm laser. In contrast, The ratio of the value of energy shift decrement of the A_1^{LO} mode is approximately two times as high as the energy decrement of E_2^H mode when heating was conducted by the Peltier device holding the sample and with a uniform temperature inside the sample. The result indicates an abnormal high-mode energy decrement in the A_1^{LO} mode. As it is known that the electrons are firstly captured by the Fe atoms, this result and the low hole mobility or diffusion length indicate the A_1^{LO} is affected by the hole plasmon, which induces the mode energy decrease because of the overdamping. When we analyze the LO mode peak of layers with high-density deep levels in Raman scattering analysis, consideration of hole plasmon is thought to be required under the condition of high-density irradiation of UV light for heating.

References

[1] D. Chowdhury, IEEE Electrification Mag. 8, 6 (2020).

[2] R. Sun, J. Lai, W. Chen, and B. Zhang, IEEE Access 8, 15529 (2020).

[3] D. W. Runton, B. Trabert, J. B. Shealy, and R. Vetury, IEEE Microw. Mag. 14, 82 (2013).

[4] K. H. Hamza and D. Nirmal, Int. J. Electron. Commun. 116, 153040 (2020).

[5] H. Amano, Jpn. J. Appl. Phys. 52, 050001 (2013).

[6] T. Sochacki, Z. Bryan, M. Amilusik, R. Collazo, B. Lucznik, J. L. Weyher, G. Nowak, B. Sadovyi, G. Kamler, and R. Kucharski, Appl. Phys. Express 6, 075504 (2013).

[7] W. Wojtasiak et al., Micromachines 9, 546 (2018).

[8] D. Zhang et al., IEEE Trans. Electron Devices 65, 3379 (2018).

[9] T. J. Anderson, M. J. Tadjer, J. K. Hite, J. D. Greenlee, A. D. Koehler, K. D. Hobart, and F. J. Kub, IEEE Electron Device Lett. 37, 28 (2016).

[10] Y. Zhang, A. Dadgar, and T. Palacios, J. Phys. D 51, 273001 (2018).

[11] J. T. Chen, C. W. Hsu, U. Forsberg, and E. Janzén, J. Appl. Phys. 117, 085301 (2015).

[12] D. F. Storm, M. T. Hardy, D. S. Katzer, N. Nepal, B. P. Downey, D. J. Meyer, T. O. McConkie, L. Zhou, and D. J. Smith, J. Cryst. Growth 456, 121 (2016).

[13] G. Koblmüller, R. M. Chu, A. Raman, U. K. Mishra, and J. S. Speck, J. Appl. Phys. 107, 043527 (2010).

[14] G. Meneghesso, M. Meneghini, and E. Zanoni, Jpn. J. Appl. Phys. 53, 100211 (2014).

[15] L. Liu, C. F. Lo, Y. Xi, F. Ren, S. J. Pearton, O. Laboutin, Y. Cao, J. W. Johnson, and I. I. Kravchenko, J. Vac. Sci. Technol. B 31, 011805 (2013).

[16] T. V. Malin et al., Tech. Phys. Lett. 45, 761 (2019).

[17] F. Chen, S. Sun, X. Deng, K. Fu, G. Yu, L. Song, R. Hao, Y. Fan, Y. Cai, and B. Zhang, AIP Adv. 7, 125018 (2017).

[18] R. P. Vaudo, X. Xu, A. Salant, J. Malcarne, and G. R. Brandes, Phys. Status Solidi A 18, 200 (2003).

[19] H. C. Chiu, S. C. Chen, J. W. Chiu, B. H. Li, R. Xuan, C. W. Hu, and K. P. Hsueh, J. Vac. Sci. Technol. B 35, 041205 (2017).

[20] S. Leone, F. Benkhelifa, L. Kirste, C. Manz, S. Mueller, R. Quay, and T. Stadelmann, Phys. Status Solidi B 255, 1700377 (2018).

[21] M. Kubota, T. Onuma, Y. Ishiihara, A. Usui, A. Uedono, S. F. Chichibu, J. Appl. Phys. 105, 083542 (2009)

[22] P. Ščajev, K. Jarašiūnas, J. Leach, J. Appl. Phys. 127, 245705 (2020).

[23] T. K. Uždavinys, S. Marcinkevičius, J. H. Evance, D. C. Look, J. Appl. Phys. 119, 215706 (2016).

[24] E. Malguth, A. Hoffmann, M. R. Phillips, Phys. Stat. Sol. B 245, 455 (2008).

[25] H. Tokuda, K. Suzuki, J. T. Asubar, M. Kuzuhara, Jpn. J. Appl. Phys. 2018, 57, 071001.

[26] Y. Arakawa, K. Ueno, H. Imabeppu, A. Kobayashi, J. Ohta, and H. Fujioka, Appl. Phys. Lett. **110**, 042103 (2017).

[27] M. Fujiwara, Y. Ishitani, X. Wang, S. B. Che, and A. Yoshikawa, Appl. Phys. Lett. **93**, 231903 (2008).

CHAPTER 6
Conclusion

The operational characteristics of III-Nitride devices are degraded by heat energy generation due to phonon generation, which leads to temperature increases in electronic devices. Phonon energy can be eliminated from the active layer, especially in the non-thermal equilibrium condition, to improve the performance of the device. These studies focus on the observation of phonon transport processes in GaInN/GaN heterostructures.

The combinations of the Raman imaging analysis of the E_2^H and A_1^{LO} or LOPC+ modes were conducted on a thin $Ga_{0.95}In_{0.05}N$ film with a thickness of 100 nm on a GaN template. The temperature increase was determined by the analysis of E_2^H mode, and the experimental value of the A_1^{LO} mode included the effects of temperature and increased electron density. According to that situation, the increased electron density can be extracted from the difference between the estimated A_1^{LO} and the experimentally observed LOPC+ energy shift. This analysis is based on the local thermal strain on the sapphire substrate without a temperature increase. This analysis enabled the study by combining the analyses of local temperature increase, LOPC, luminescence intensity, and the local photoemission efficiency per electron or hole obtained. There is a limitation of PL analysis to obtain information of the carrier density, especially in materials with spatially nonuniform alloy composition distribution. This present analysis assists to obtain the information of the carrier density. In addition, it will provide a deeper understanding of the interaction between recombination processes and thermal effects. The simultaneous imaging of PL intensity, carrier density, and temperature provides the details of local carrier dynamics, including both radiative and

nonradiative recombination rates. This comprehensive approach assists in understanding the interactions within the nonuniformity alloy composition of nitride materials.

In addition, thermal energy transport at the heterointerfaces of $Ga_{1-x}In_xN$/GaN was studied using a microscopic Raman measurement system with two laser systems. The 532 nm laser observed the GaN layer and 325 nm provided as a heating laser at the GaInN layer to investigate thermal energy transport across the heterointerfaces. In this study, higher energy transport was observed at the $Ga_{1-x}In_xN$/GaN heterointerface with a graded variation in x (0~0.17) compared to the $Ga_{0.91}In_{0.09}N$/GaN heterointerface, despite the average InN fraction *x* of 0.085 for sample B being nearly identical to the *x* of 0.09 for sample A. The high thermal energy transport is attributed to the higher phonon transport from the lower phonon energy gap at the heterointerface. Therefore, the mechanism of the phonon transport analysis can be investigated in this study by using the two lasers system.

Furthermore, Fe-doped GaN and bulk GaN were studied using two heating conditions of thermal equilibrium and laser heating in Raman spectroscopy. The ratio of the value of energy decrement in A_1^{LO} mode is five times as high as the energy decrement in E_2^H mode or higher when heating by the 325 nm laser. In contrast, The ratio of the value of energy shift decrement of the A_1^{LO} mode is approximately two times as high as the energy decrement of E_2^H mode when heating was conducted by the Peltier device holding the sample and with a uniform temperature inside the sample. The result indicates an abnormal high-mode energy decrement in the A_1^{LO} mode. An abnormal high mode energy shift to the lower energy side is observed for the laser-heating condition for the A_1(LO) mode but not for the E_2(high) mode. This phenomenon is more significant for samples with higher Fe densities. Thus, that phenomenon can be attributed to the energy shift of the higher energy branch of the LOPC modes to the lower energy side, which is possible for the coupling with hole-plasmon. This result suggests the domination of hole density in the photo-excited area by the fast capture of electrons by Fe atoms. The low hole mobility or diffusion length indicate the A_1^{LO} is affected by the hole plasmon, which induces the mode energy decrease because of the overdamping. When we analyze the LO mode peak of layers with high-density deep levels in Raman scattering analysis, consideration of hole plasmon is thought to be required under the condition of high-density irradiation of UV light for heating.

These studies allow us to study the effect of phonon transport or cooling of lattices on the carrier dynamics, electronic temperature, and radiation efficiency of the electronic band-to-band transition.

LIST OF FIGURES

CHAPTER 1

CHAPTER 2

CHAPTER 3

LIST OF TABLES

LISTS OF PUBLICATION AND PRESENTATION

PUBLICATIONS

1. **Thee Ei Khaing Shwe**, Tastuya Asaji, Ryota Kimura, Daisuke Iida, Mohammed A. Najmi, Kazuhiro Ohkawa, and Yoshihiro Ishitani, "*Photoluminescence Emission Efficiency Analysis Methodology by Integrating Raman Spectroscopy of the A_1(LO) and E_2(high) Phonons in a GaInN/GaN Heterostructure*", phys. Status Solidi B 2004, 2400057, 10 pages, 2024.04.27.
2. **Thee Ei Khaing Shwe**, Tatsuya Asaji, Daisuke Iida, Mohammed A. Najmi, Kazuhiro Ohkawa, and Yoshihiro Ishitani, "Local augmentation of phonon transport at GaInN/GaN heterointerface by introducing a graded variation of InN mole fraction", Appl Phys. Lett. 125, 012105(2024), 7 pages, 2024.07.01.

CONTRIBUTION PUBLICATION

1. Bojin Lin, Hnin Lai Lai Aye, Koichi Seimiya, **Thee Ei Khaing Shwe**, Tatsuya Asaji, Yoshihiro Ishitani, "Damping effect of longitudinal optical phonon-plasmon coupling on thermal radiation from surface micro-gratings on direct and indirect electronic transition type semiconductors", Appl. Phys. Lett. 124, 032102 (2024), 6 pages, 2024.01.18.

PRESENTATION

1. **Thee Ei Khaing Shwe**, Tomoya Nakayama, Tastuya Asaji, Daisuke Iida, Mohammed A. Najmi, Ryota Kimura, Yuki Kikuchi, Kazuhiro Ohkawa, and Yoshihiro Ishitani, "*Thermal energy transport in different alloys composition with Raman Scattering*", The 70th JSAP Spring Meeting 2023.

2. **Thee Ei Khaing Shwe,** Tastuya Asaji, Ryota Kimura, Yuki Kikuchi, Daisuke Iida, Mohammed A. Najmi, Kazuhiro Ohkawa, and Yoshihiro Ishitani,"Dynamics comparison of E_2(H) and A_1(LO) modes in InGaN/GaN heterostructures", The 7th Phonon Engineering Workshop 2023.

3. **Thee Ei Khaing Shwe**, Tastuya Asaji, Ryota Kimura, Yuki Kikuchi, Daisuke Iida, Mohammed A. Najmi, Kazuhiro Ohkawa, and Yoshihiro Ishitani,"*Longitudinal optical phonon dynamics analysis in GaInN/GaN heterostructures by Raman spectroscopy*", International Conference on Nitride Semiconductors (ICNS2023).

4. **Thee Ei Khaing Shwe,** Tastuya Asaji, Bei Ma, Daisuke Iida, Mohammed A. Najmi, Kazuhiro Ohkawa, and Yoshihiro Ishitani,"Integrated analysis of the A_1(LO) and E_2(high) modes in GaInN/GaN heterostructures by Raman Spectroscopy", The 71st JSAP Spring Meeting, 2024.

5. **Thee Ei Khaing Shwe,** Tastuya Asaji, Bei Ma, Daisuke Iida, Mohammed A. Najmi, Kazuhiro Ohkawa, and Yoshihiro Ishitani , "Analysis of phonon transport at GaInN/GaN heterointerface by double laser Raman Spectroscopy" The 31st of Laser Summer School,2024.

6. **Thee Ei Khaing Shwe,** Tastuya Asaji, Bei Ma, Daisuke Iida, Mohammed A. Najmi, Kazuhiro Ohkawa, and Yoshihiro Ishitani , "Condition of phonon transport augmentation at GaInN/GaN heterointerface" The 85th JSAP Autumn Meeting, 2024.

7. **Thee Ei Khaing Shwe,** Daisuke Iida, Tatsuya Asaji, Mohammed A. Najmi, Bei Ma, Kazuhiro Ohkawa, and Yoshihiro Ishitani , "Analysis of phonon transport at GaInN/GaN heterointerface by two lasers system with Raman spectroscopy" The 11th International Conference on Science and Engineering, 2024.

8. **Thee Ei Khaing Shwe,** Kohei Ueno, Bei Ma, Hiroshi Fujioka, and Yoshihiro Ishitani, "Integrated analysis of the ratio of A_1(LO) and E_2(high) modes energy shift in Fe-doped GaN with Raman spectroscopy", The 72nd JSAP Spring Meeting, 2025.